

CHALMERS



Measurements and Prediction of Laminar- Turbulent Transition at High Free-Stream Turbulence in Boundary Layers with Pressure Gradients

BERCELAY MAURICIO NIEBLES ATENCIO

Department of Applied Mechanics
Division of Fluid Dynamics
CHALMERS UNIVERSITY OF TECHNOLOGY
Göteborg, Sweden 2011
Master's thesis 2011:37

MASTER'S THESIS 2011:37

Measurements and Prediction of Laminar-
Turbulent Transition at High Free-Stream
Turbulence in Boundary Layers with Pressure
Gradients

BERCELAY MAURICIO NIEBLES ATENCIO

Department of Applied Mechanics
Division of Fluid Dynamics
CHALMERS UNIVERSITY OF TECHNOLOGY
Göteborg, Sweden 2011

Measurements and Prediction of Laminar-Turbulent Transition at High Free-Stream
Turbulence in Boundary Layers with Pressure Gradients

BERCELAY MAURICIO NIEBLES ATENCIO

© BERCELAY MAURICIO NIEBLES ATENCIO, 2011

Master's Thesis 2011:37

ISSN 1652-8557

Department of Applied Mechanics

Division of Fluid Dynamics

Chalmers University of Technology

SE-412 96 Göteborg

Sweden

Telephone: + 46 (0)31-772 1000

Printed at Chalmers Reproservice
Göteborg, Sweden 2011

Measurements and Prediction of Laminar-Turbulent Transition at High Free-Stream Turbulence in Boundary Layers with Pressure Gradients

Master's Thesis by
BERCELAY MAURICIO NIEBLES ATENCIO
Department of Applied Mechanics
Division of Fluid Dynamics
Chalmers University of Technology

ABSTRACT

The laminar-turbulent transition has significant influence on determining the aerodynamic characteristics of immersed bodies such as evolution of losses, the appearance of separation and stall. Also, the transition behavior has a dominant effect on the distributions of wall shear stress and surface heat transfer. To predict and manage the turbulence in different flow cases is beneficial for optimum advantage, namely, to reduce it when it is harmful (e.g. to decrease the skin friction or heat transfer) and to increase it when it is desirable (to avoid flow separation). The prediction of transition at high free-stream turbulence is of particular importance in turbomachinery where the boundary layer state defines the blade heat transfer and the flow separation margins.

This project report presents a study on measurements and prediction of laminar-turbulent transition at high free-stream turbulence in boundary layers of the airfoil-like geometries with presence of the external pressure gradient changeover. The experiments are performed for a number of flow cases with different flow Reynolds number, turbulence intensity and pressure gradient distributions. The results were then compared to numerical calculations for same geometries and flow conditions. The experiments and computations are performed for the flow parameters which are typical for turbomachinery applications and the major idea of current study is the validation of the turbulence model which can be used for such engineering applications.

Key words: Aerodynamics, Laminar-Turbulent Transition, High Free-Stream Turbulence, Shear Stress, Heat Transfer, Turbulence, Flow Separation, Turbomachinery, Laminar, Pressure Gradient, Experiments

Preface

In this project, some tests have been done to find out the effect of certain flow parameters on the transition onset phenomena. The tests have been carried out from April 2011 to May 2011. These studies arose from the need to understand this extraordinary process, especially for engineering applications. The project was carried out at the Department of Applied Mechanics, Fluid Dynamics, Chalmers University of Technology, Sweden.

This project has been supervised by Associated Professor Dr. Valery Chernoray and Guest Professor Dr. Mohsen Jahanmiri (from Shiraz University in Iran). All tests have been carried out in the Wind Tunnel Laboratory of the Applied Mechanics Department at Chalmers University of Technology.

I would like to express my gratitude to God and our Lord Jesus Christ for all their blessings. My supervisors and the Fluid Dynamics staff for their great guidance, collaboration and wonderful work environment. Finally, I thank my family, friends and classmates for their support and understanding.

Göteborg, June 2011

Bercelay Mauricio Niebles Atencio

Notations

Roman upper case letters

C_p	Pressure Coefficient
K	Acceleration parameter
H_{12}	Shape Factor
Re	Local Reynolds number
Re_θ	Reynolds number based on the momentum thickness
Tu	Turbulence intensity of the freestream, per cent
U	Velocity of the freestream

Roman lower case letters

dy	Differential of the distance from the wall in the boundary layer
dU	Differential of the velocity in x -direction
dx	Differential of positions in the streamwise direction
u	Flow velocity inside the boundary layer
x	Coordinate in the streamwise direction
y	Coordinate normal to the surface
z	Coordinate in the spanwise direction

Lower case Greek

δ^*	Displacement thickness
θ	Momentum thickness
λ_θ	Pressure gradient parameter
ν	Kinematic viscosity

Subscripts

t	Beginning of transition
∞	Freestream value
0	Surface value
ref	Reference
<i>rms</i>	RMS
max	Maximum

Abbreviations

CAD	Computer Aided Design
CCA	Constant Current Anemometer
CTA	Constant Temperature Anemometer
DNS	Direct Numerical Simulation
PC	Personal Computer
RMS	Root Mean Square
T-S	Tollmien–Schlichting (waves)

CONTENTS

ABSTRACT	I
PREFACE	III
NOTATIONS	V
1 INTRODUCTION	1
2 THEORETICAL REVIEW	5
2.1 Boundary Layers	5
2.2 Transition	7
2.2.1 Types of Transition	9
2.2.2 Effect of Pressure Gradient on Transition Onset	10
2.2.3 Effect of Curved Surfaces on Transition Onset	10
2.3 The Hot Wire Anemometer	11
2.3.1 Modes of Operation of Hot Wire Anemometers	11
3 EXPERIMENTAL ASPECTS	14
3.1 Design of Experimental Models	14
3.2 Experimental Set-up	14
3.3 Data Processing Technique	19
4 RESULTS	20
4.1 Pressure Distribution	20
4.2 Effect of Flow Reynolds Number	21
4.3 Effect of Pressure Gradient	25
4.4 Effect of Free-Stream Turbulence Intensity	27
4.5 Filtered RMS	30
4.6 Comparison of CFD Calculations and Experiments	33

CONSLUSIONS	37
REFERENCES	38
APPENDIX	40

CHAPTER 1

INTRODUCTION

No flow in nature and engineering applications is disturbance-free. The disturbances present in the flow field may enter the boundary layer via its boundaries, which may be the wing surface and the edge separating the layer from the free stream. An example is the roughness or vibrations of a wing surface, the sound waves or eddies in the free stream. These disturbances may transfer energy to the boundary layer and establish boundary-layer instabilities which may amplify and attain amplitudes far above those of the external disturbances. The sensitiveness of the boundary layer to external disturbances is called Receptivity. Once these disturbances are present in the flow, a different behavior is often the consequence.

The transition from laminar to turbulent flow is a series of processes by which a flow, generally by increasing its Reynolds number, passes from laminar or regular regime to turbulent or irregular regime. Understanding the transition is very important for the efficient turbulence control. Knowing how, when and where this process takes place is beneficial in cases where the turbulence is necessary to be avoided (in cases when it is harmful), but also in cases where the turbulence might be desirable to promote, for instance, better fluid mixing or in other words, to manage turbulence efficiently. It is also known there is a strong relation between transition and flow separation, which is a non-desirable phenomena in most of the engineering applications. Therefore, understanding the transition may lead to a better control of separation.

Rayleigh established in 1880, that transition is a stability problem of the flow which can be seen as a dynamic system subject to perturbations or disturbances. When these disturbances cannot be attenuated the stability is lost. The process by which disturbances penetrate the boundary layer and create instabilities is named “receptivity”. Initially, small amplitude T-S waves are generated but when the amplitude increases, secondary instabilities promote the transition to turbulence.

The receptivity phenomenon has been studied by many researchers, but it is not completely understood and more investigation is needed. Schrader, Brandt et al [1] have found that the boundary layers in blunt leading edges are more receptive to axial free stream vortices with low frequencies and in this process non-modal instabilities are generated. Also, in the case of vertical free stream vortices, non-modal instabilities are created for low amplitudes. In this case, the vortices pass from being vertical to axial due to the effect of vortex stretching and tilting. They have also found that span wise vortices trigger T-S instability through wavelength reduction of the upstream boundary-layer disturbance due to non-parallel effects at the leading edge. Finally, they observed an adverse pressure gradient following the acceleration on the nose

causes the most pronounced effects on the instability development. Other works have been conducted in receptivity. Saric et al [2] reviewed the leading edge receptivity to external disturbances when produced by sound and found validation of theory aspects of transition, due to the agreement between theory and experiments on 2-D roughness. They also found agreement between theory and experiments in regard to leading edge receptivity coefficients and concluded that the experiments together with DNS simulations are highly important for providing relevant information to help in the understanding of leading edge receptivity.

The transition phenomenon as such has also been investigated previously for sharp leading edge plates but a unique relation between the transition Reynolds number and turbulence has not been completely well defined, because some other parameters play an important role in the transition boundary layer, such as turbulence intensity of free stream, streamline curvature, flow pressure gradient, etc. In a recent work, Zhigulev, Uspenskii and Ustinov [3] studied the effect of turbulence scale and leading edge shape on laminar-turbulent transition in the flat plate boundary layer due to grid and found that for plates with sharp edges, the fluctuation growth and the laminar-turbulent transition point depend non-monotonically on the turbulence scale.

In trying to understand the transition process, plenty of data and information has been collected from experiments in flat plates, but not much information and data has been collected and is available when it comes to understand the effect of free stream turbulence levels in the development of boundary layers along an airfoil or a vane, which is worthy to say that has a quite large application in engineering. Randomsky and Thole [4] presented measurements of the mean and turbulent flow field in the inviscid region of a turbine blade for low and highly turbulent flow field. They showed that in the inviscid region, the turbulent kinetic energy remains relatively high and also found some augmentation of the heat transfer near the leading edge and the pressure side as well, due to the high turbulence level. The same authors in another paper [5], show that for laminar profiles, the mean velocity profiles seemed to be consistent, but when it came to high free stream turbulent conditions, large velocity fluctuations in the pressure side of the airfoil were observed. They also found that the transition moved upstream in the suction side due to free stream turbulence.

The nature of the transition itself allows the identification of turbulent/non-turbulent patterns which were first observed by Corrsin in 1943 [6]. This phenomenon was termed intermittency and later on, Kovaszny et al. [7] introduced the intermittency factor to identify turbulence, so that it is one when the fluid is turbulent and zero otherwise.

Maybe one of the best papers regarding the study of the effect of pressure gradients and turbulence levels on transition is the one authored by Abu-Ghannam and Shaw [8] proposing methods to calculate the momentum thickness Reynolds number for the

start and the end of the transition zone, defined by them as the region in which the intermittency factor ranges between 0.25 and 0.75.

Some other studies in transitional boundary layers subjected to different pressure gradients and turbulence levels have been carried out: Gostelow et al [9] found that at strong adverse pressure gradients, transition occurs quickly but it seems that the velocity profiles do not reflect this before the transition is completed. In another paper, Gostelow and Walker [10] carried out experiments under high turbulence levels and adverse pressure gradients and found that close to the wall region within the boundary layer, a turbulent pattern was found to be not much affected by the free-stream conditions. The outer part of the boundary layer is more strongly affected by turbulence level and pressure gradient. Finally, in another paper together with Salomon [11], the same researchers presented a new method for calculating intermittency in transitional boundary layers with rapidly changing pressure gradients, which is based on experimental studies using the pressure gradient parameter. Johnson and Ercan [12] also presented a new method for predicting boundary layer transition by modeling the near the wall fluctuations of velocity induced in the laminar boundary layer.

Mayle in his well-known paper, [13] mentions some experiments performed by Görtler in 1940 and Liepman in 1943, who analyzed the effect of curvature on transition. From the experiments carried out by the latter, the transition Reynolds number depends on the turbulence level and on how strong the curvature is and seems to have a non-negligible effect in low pressure turbines and small engines, where a delay can be found. For compressors, the effects are negligible but still more data and studies are needed. In the same paper, Mayle keeps the discussion regarding the effect of curvature on transition and by using a curvature parameter, analyses its influence on transition Reynolds number. Moreover, he goes through the transition in different components based on what has been observed and found by other researchers and designers.

Other researchers such as Bario and Beral [14] presented in their paper the results of their boundary layer measurements on pressure and suction sides of a turbine inlet blade and found on the pressure side that the onset of the transition, for low turbulence levels, occurs when Görtler vortices have been found. On the other hand, for high turbulence levels, the transition occurs at the beginning of the pressure side. The turbulence effect in the pressure side is considerable compared to that of the suction side. On the suction side, for low turbulence levels, the transition occurs before the flow may get separated and for higher levels of turbulence, the transition moves upstream to the leading edge.

Van Treuren et al [15] conducted experiments in the suction side of a low pressure inlet turbine for low free stream turbulence level and high free stream turbulence levels. In both cases they worked with low Reynolds numbers (25000 and 50000). At the lowest end of this range, they found strong and steady separation unable to be

corrected either increasing the turbulence level or using vortex generator jets. When they worked with Reynolds number 50000, strong separation of the flow downstream the suction side of the vane was found for low free stream turbulence levels, but also they found opportunities to reattach the flow by introducing vortex generators and when increasing the turbulence levels.

In spite of the previously mentioned works, more information and study has to be performed in order to understand the effect of the different variables on the transition process over the airfoils, vanes and blades, which are, as previously said, present in many engineering applications. The aim of this project is therefore, to perform experiments in the conventional wind tunnel of the Department of Applied Mechanics at Chalmers University of Technology with the help of the hot-wire measurement systems to investigate the effect of nose radius variation on the transition point and heat transfer rate of an ellipsoid to simulate and generalize the results.

CHAPTER 2

THEORETICAL REVIEW

2.1 Boundary Layers

As an object moves through a fluid or when the fluid is moving past an object, the fluid particles are disturbed and forced to move around the object, creating aerodynamic forces between the object and the fluid. These forces depend in magnitude on some factors such as the shape and of the object, the mass flow passing by the object and on two quite important fluid properties, which are the viscosity and the compressibility.

There is a complex dependency of the aerodynamic forces on the viscosity of the fluid. As the fluid moves past the object, some fluid particles which are right next to the object stick to the surface and those just above the surface are slowed down due to the collisions with the fluid particles sticking to the surface. In turn, these particles slow down the ones passing above them. This process occurs continuously and the farther one moves away from the surface, the fewer the collisions due to the object surface presence. A thin layer of fluid is then created in which the velocity changes from zero at the surface to the free stream value away from the surface. This is the so called boundary layer.

The flow within this layer could be either laminar (for low Reynolds number), or turbulent (high Reynolds number) and the manner in which the velocity changes through the layer is shown as indicated on Figure 1 by the velocity profiles. Unlike the laminar profile which grows slowly, the turbulent boundary layer profile is much fuller with a rapid increase of the velocity close to the object surface. The difference in these profiles is due to the viscous forces. In the laminar case, these forces are parallel to the flow direction, leading to a gradual increase in velocity between the layers. In the turbulent case, fluctuations in all directions appear causing an exchange of momentum between layers and as a consequence, the velocity profile is more uniform than the laminar case.

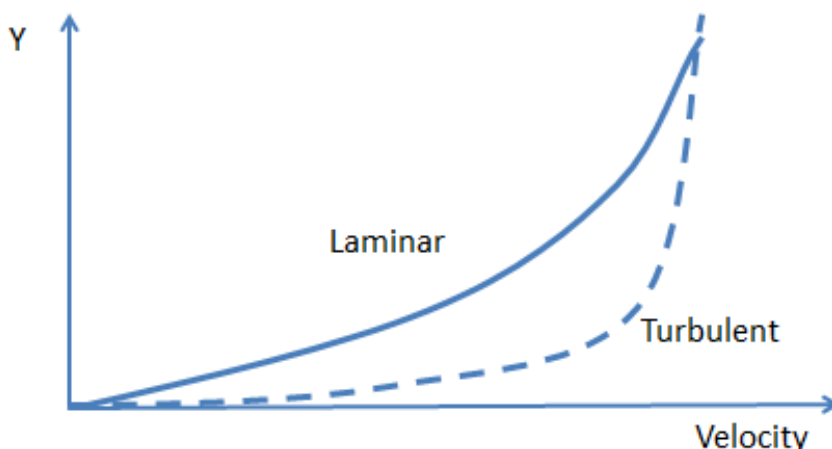


Figure 1: Laminar and Turbulent velocity profiles

Frictional forces always try to introduce rotation between the particles in motion, but the viscosity at the same time prevents the rotation to occur. Depending on the relative value of these forces we can have different flow states.

When the shear rate is low, the inertial force is greater than the friction and the fluid particles move but not rotate, or do so with quite small energy. The result is a movement in which these particles follow defined paths and all those passing through a point in the flow follow the same path. The flow is laminar.

By increasing the shear rate, the friction between neighboring molecules to the fluid increases and these acquire a significant rotational energy. The viscosity is lost and due to the rotation, a change in career is experienced by the molecules, increasing collisions and the change of direction. The flow is now turbulent. It is worthy to mention that a laminar sublayer, also called the viscous sublayer, is formed at this region of mainly-turbulent flow which is near the no-slip boundary. The existence of such sublayer can be explained taking into account that the flow velocity decreases towards the no-slip boundary, where the influence of the viscosity the largest. Because of this, the Reynolds number decreases until at some point the flow crosses the threshold from turbulent to laminar. Generally speaking, the viscous sublayer extends from the surface to a distance of about 10 to 20% of the boundary layer thickness and can be separated mainly into two regions: a linear sublayer where velocities vary linearly from the wall and the viscous forces are much larger in magnitude than the turbulent shear stresses, and the other region in the viscous layer is the buffer layer in which the viscous and forces and turbulent shear stresses are the same magnitude. Figure 2 shows a boundary layer sketch and its basic features.

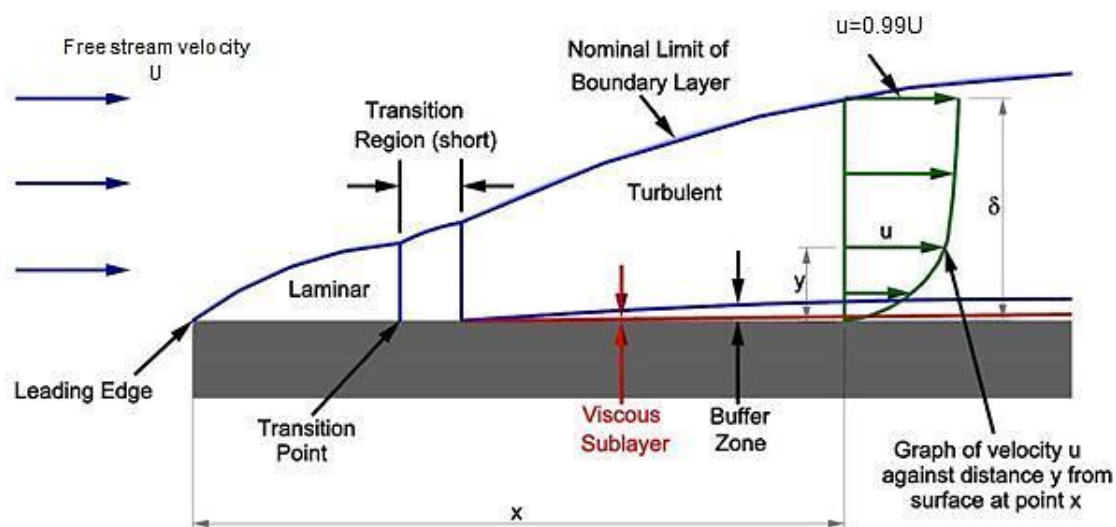


Figure 2: Features in boundary layers, from [16]

The thickness of a boundary layer has been defined in different ways. One of these definitions considers the boundary layer thickness from the point of zero velocity (at the surface of the object) up to the point where the velocity of the flow within the boundary layer is 99% of the main flow velocity. Another definition of boundary layer thickness introduces the term displacement thickness δ^* , which is the distance that the outer streamlines deflecting outwards due to the presence of the object's boundary layer. Finally, the momentum thickness, θ , is referred as the distance the object should move parallel to itself in the inviscid fluid stream in order to get the

same momentum as the one existing in the viscous fluid. In Figure 3 it is possible to see graphically the displacement thickness definition.

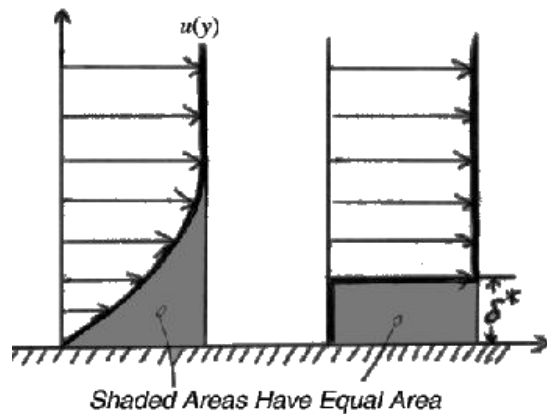


Figure 3: Displacement thickness sketch, from [17].

δ^* and θ are calculated with the flow velocity in the boundary layer u and freestream velocity U :

$$\delta^* = \int_0^{\infty} \left(1 - \frac{u}{U}\right) dy$$

$$\theta = \int_0^{\infty} \frac{u}{U} \left(1 - \frac{u}{U}\right) dy$$

The boundary layer may lift off or "separate" from the body creating an effective shape quite different from the physical shape. This happens when the flow, in relation to the free stream, has very low energy and is more easily driven by pressure changes. The effects of the boundary layer on lift are contained in the lift coefficient and the effects on drag are contained in the drag coefficient. The shape factor H_{12} defines the nature of the flow and is the ratio between displacement thickness and momentum thickness. High values for H_{12} indicate strong adverse pressure gradient and higher risk of separation [18].

2.2 Transition

Transition is a series of processes which take place and make a certain flow pass from laminar regime to turbulent. The existence of disturbances in the flow is a necessary condition for the transition to occur. However, that instability does not lead inexorably to transition and there might be a significant streamwise distance between laminar and transitional flows. If disturbances die away in time, the flow is said to be stable. Otherwise, the flow is unstable and the possibility of transition increases greatly.

Current studies are devoted to identify conditions for inception and development of disturbances. It is of particular interest, for example, to predict accurately the

Reynolds number at which the disturbances are amplified and transition to fully turbulent flow takes place.

Transition is mainly affected by Reynolds number, but also pressure distribution, roughness and turbulence intensity of the outer flow. At low turbulence of the incoming flow the transition occurs as depicted in Figure 4, which is taken from Versteeg and Malalasekera [19]. When a disturbance is present in the flow, the so-called unstable Tollmien-Schlichting (T-S) waves are developed in the flow, which are originally two dimensional (2-D), amplified in the flow direction and described by linear theory (these are the primary instabilities). These disturbances grow slowly until the wave is about at 1 or 2% of the free stream velocity. The amplification takes place over a limited range of Reynolds number. Therefore, a downstream attenuation of the amplified waves is possible and the flow consequently, remains as laminar. As the amplitude increases, the disturbances become inexorably three dimensional (3-D) and the linear theory is no longer able to describe its behavior. These disturbances lead to Λ -structures or vortices, which are commonly aligned originating the K-type transition. A high shear region is induced and then intensified, elongated and rolled up. Further, a cascading breakdown of the high shear layer into smaller units are followed by the generation of the so called turbulent spots, which then merge downstream forming the turbulent flow.

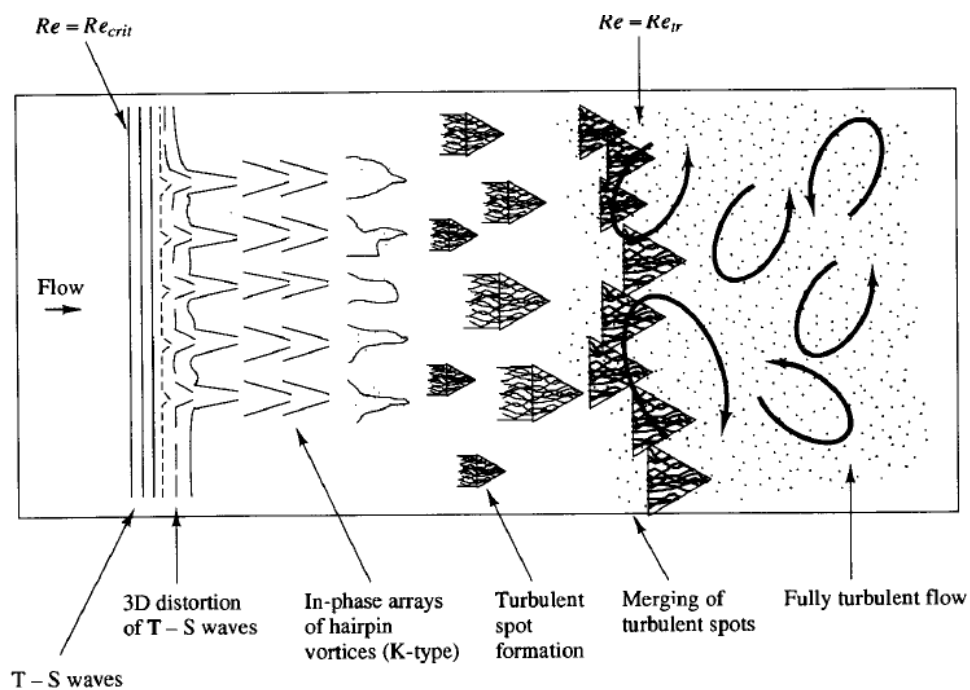


Figure 4: Disturbance development during natural transition in boundary layers.

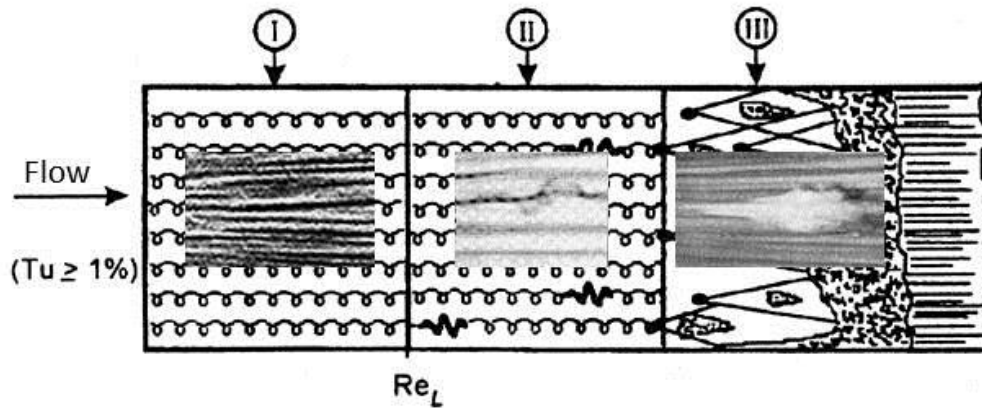


Figure 5: Disturbance development during by-pass transition [20].

2.2.1 Types of Transition

Some important processes have been identified and Mayle [13] mention them in his paper in 1991:

- **Natural transition** is the mode most thought of when “transition” is mentioned, and this occurs as a weak instability grows in a laminar boundary layer until subsequent breakdown and formation of turbulence. This process involves the completion of several stages. Summarizing, these are: 1) The Reynolds number momentum thickness reaches a critical value ($Re_{\theta t}$) at which the boundary layer becomes susceptible to small disturbances, developing instabilities in the form of the two-dimensional T-S waves, which 2) grow and develop into three-dimensional instabilities. 3) These instabilities continue growing and end up into high fluctuation vortices. Finally, 4) these vortices develop into turbulent spots, which coalesce downstream into a fully developed turbulent boundary layer.
- **Bypass transition** where some or the entire laminar breakdown process does not occur, and is instead driven by free stream unsteadiness. In other words, some of the stages in natural transition may be bypassed, particularly in the presence of large free-stream disturbances, the presence of side walls or large roughness. In this case, the turbulent spots are directly formed within the boundary layer due to the free stream unsteadiness. Since the first stages are bypassed, linear instability is irrelevant and no T-S waves are found. Figure 5 displays the major transition stages for this case. (I) The initially laminar boundary layer is modulated by longitudinal streaks. (II) The high-frequency wave packets are generated and the incipient spots are formed as the Reynolds number exceeds a critical level. (III) The turbulent spots are developed and merged.
- **Separated-flow transition** occurs when a laminar boundary layer separates and transitions in the free-shear-layer-like flow near the surface. In this case, the flow reattaches as a “bubble” on the surface. This type of transition can occur near the leading edges of blades and near the point of minimum pressure

on the suction surface sides. Of all of the modes, separated-flow transition is the most crucial for compressor and low pressure turbine design. By a proper understanding and utilization of separated-flow transition through separation bubbles, an increase of low pressure turbines, compressors and small-engines turbines efficiency may be reached.

- **Reverse transition**, often called “relaminarization”, occurs where a previously turbulent or transitional region is affected, usually by a strong favorable pressure gradient, so it becomes laminar. An instantaneous snapshot of the flow over a single airfoil may include laminar flow near the leading edge, followed by a wake-or shock-induced transition which is in turn replaced by a relaminarization with subsequent transition to turbulence occurring at multiple locations simultaneously.

2.2.2 Effect of Pressure Gradient on Transition Onset

Continuing with Mayle, in the same paper an analysis of the pressure gradient effect on boundary layer transition is presented. The onset of transition and its length is normally presented in terms of the pressure gradient parameter, $\lambda_\theta = (\theta^2/\nu)(dU/dx)$ especially for natural transition processes. This parameter however, seems to be not very appropriated for other forms of transition and the acceleration parameter $K = (\nu/U_t^2)(dU/dx)$ is used instead, especially for flows with favorable pressure gradients.

In general, Re_{θ_t} is increased either by increasing acceleration or by decreasing the free stream turbulence intensity. For low turbulence intensities, the effect of acceleration is strong but for some engineering applications such as gas turbines, the turbulence intensity prevails on transition.

Another conclusion worthy to mention from Mayle’s paper is that the effect of free stream turbulence intensity on transition is much stronger for favorable pressure gradient flows than adverse pressure gradients.

Abu-Ghannam and Shaw [8] are two of the few researchers who have conducted studies in non-zero pressure gradients. They found that for decreasing adverse pressure gradients, the Reynolds number momentum thickness at start of transition decreases as the reference velocity increases. At lower reference velocities, the transition starts further downstream.

2.2.3 Effect of curved surfaces on Transition onset

Finally, Mayle mentions experiments performed by Görtler (1940) and Liepman (1943) which according to their observations, the onset of transition on a convex surface is somehow similar to that for a flat plate at high free-stream turbulence levels.

From experiments carried out by Liepman (1943), a concave curvature could either decrease or increase the transition Reynolds number depending on the turbulence level and the curvature strength. The curvature seems to have negligible effects on the transition onset in all cases except probably in small engines and low turbines of

medium sized engines where it could cause a delay. For compressors, the effect of curvature could be neglected, since their blade curvatures are basically larger than those for turbines. However, more data and study are required, keeping this issue as a pending task.

2.3 The Hot Wire Anemometer

It is versatile technique used for measuring velocity and temperature fluctuations in the time domain for investigations in turbulent flows. This technique is useful for over wide speed ranges from low subsonic to high supersonic flows. This is an intrusive method capable of detecting turbulent perturbations and measuring of instantaneous velocities and temperatures at a point in a flow with a large dynamic response because of the small hot-wire thermal inertia and its correction in the anemometer.

The advantages of using this technique are listed as follows:

- Good frequency response: measurements to several hundred kHz possible, 1 MHz also feasible.
- Velocity measurement: measures magnitude and direction of velocity and velocity fluctuations, wide velocity range.
- Temperature measurements
- Two phase flow: measurements in flows containing continuous turbulent phase and distributed bubbles.
- Signal to noise ratio: have low noise levels. Resolution of 1 part in 10000 is accomplished.
- Signal analysis: output is continuous analogue signal, both time domain and frequency domain analysis can be carried out. Output can also be processed by digital systems.
- Measurement of turbulent quantities like vorticity, dissipation rate etc.

But at the same time, this technique has some drawbacks which are:

- Intrusive technique: modification of local flow field
- High turbulence-intensity flows:
 - Errors due to neglecting higher order terms
 - Rectification error – insensitive to reversal of flow direction.
- Contamination: deposition of impurities in flow on sensor alters the calibration characteristics and reduces frequency response.
- Probe breakage and burn out
- Unable to fully map velocity fields that depend strongly on space coordinates and simultaneously on time.
- Spatial array of many probes would be required.
- Fails in hostile environment like combustion.

2.3.1 Modes of Operation of Hot Wire Anemometers

Constant Current Anemometer (CCA): where the current is kept constant and variations in wire resistance caused by the flow are measured by monitoring the voltage drop variations across the filament.

Constant Temperature Anemometer (CTA): The temperature and hence the Resistance of the wire is kept constant by using a servo amplifier. The measurable signal when a change in flow velocity occurs is the change in current to be fed to the sensor.

Since the CTA is the technique used for the experiments carried out for this study, more details on it will be further mentioned.

The CTA anemometer operates on the basis of convective heat transfer from a heated sensor to the surrounding fluid, the heat transfer being primarily related to the fluid velocity.

The velocity sensor is heated to an elevated, relative to the surroundings, temperature by means of control electronics. Typical measuring equipment constitutes a measuring chain. In the hot-wire anemometer guide [21] the measuring chain is explained: it consists typically of a Probe with Probe support and Cabling, a CTA anemometer, a Signal Conditioner, an A/D Converter, and a Computer. Dedicated application software is used for CTA set-up, data acquisition and data analysis. A traverse system is used for probe traverse in space. Probe calibration can either be performed *in situ* or in a dedicated probe calibrator. See Figure 6.

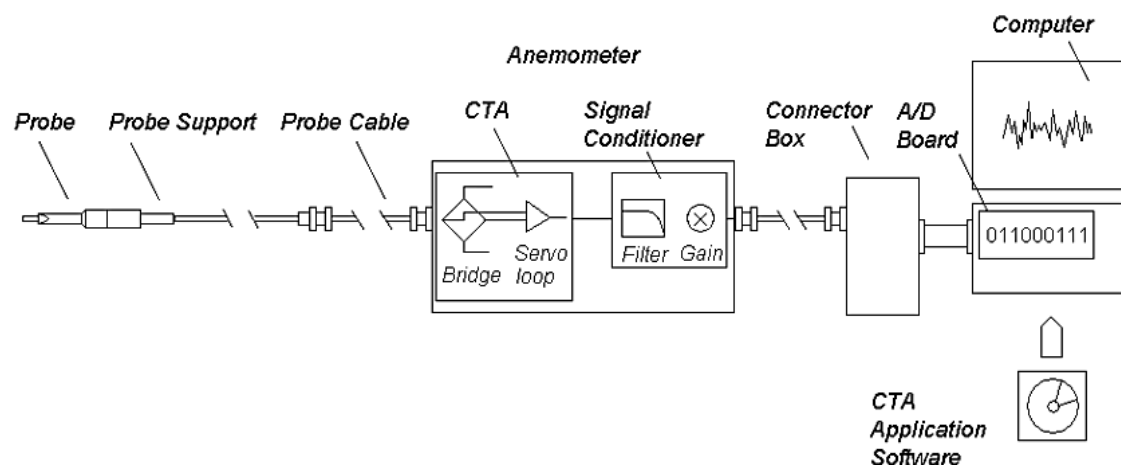


Figure 6: Typical CTA measuring chain, [21].

The hot-wire sensor is operated by a Wheatstone bridge. The circuit tries to keep the error voltage zero (the resistances of the two lower legs of the bridge match) by means of an operational amplifier. Air (or another fluid) flowing past the velocity sensor (probe) tends to cool it, which results in decreasing sensor resistance. The operational amplifier responds by immediately and delivers more power to the top of the bridge to maintain the temperature (resistance) constant. As more air flows past the sensor, more electrical power is required to maintain a balanced bridge. Thus, the faster the air, the higher the output voltage. This is the basic principal of operation for constant temperature anemometers, see Figure 7.

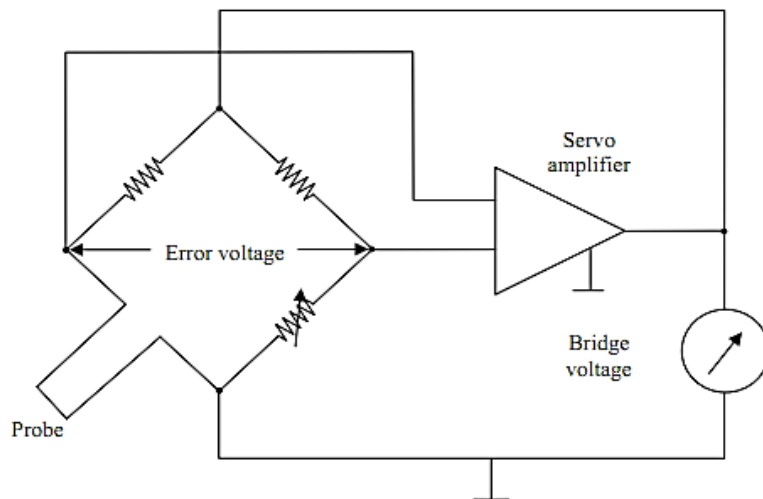


Figure 7: Sketch representing the operating principle of the CTA hot wire anemometer [22]

The Hot Wire Anemometer guide previously mentioned also explains basic types of sensors. The anemometer probes are available with four types of sensors: Miniature wires, Gold-plated wires, Fiber-film and Film-sensors. Wires are typically 5 μm in diameter and 1.2 mm long suspended between two needle-shaped prongs (Figure 8a). Gold-plated wires have the same active length but are copper- and gold-plated at the ends to a total length of 3 mm long in order to minimize prong interference (Figure 8b). Fibre-sensors are quartz-fibers, normally 70 μm in diameter and with 1.2 mm active length, covered by a nickel thin-film, which again is protected by a quartz coating (Figure 8c). Fibre-sensors are mounted on prongs in the same arrays as are wires (Figure 8d). Film sensors consist of nickel thin-films deposited on the tip of aerodynamically shaped bodies, wedges or cones.

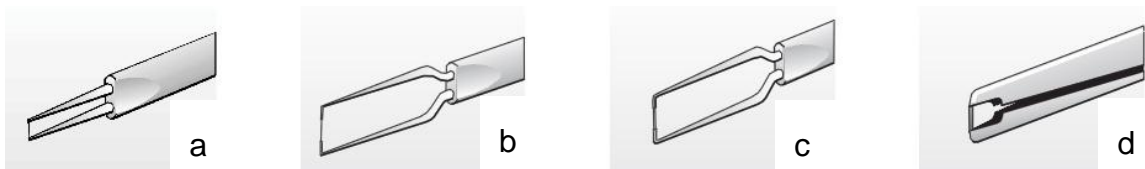


Figure 8: Types of sensors for hot wire anemometers.

CHAPTER 3

EXPERIMENTAL ASPECTS

3.1 Design of Experimental Models

For designing the experimental models some factors were taken into consideration: its geometry should be as simple as possible, easy to manufacture and to place in the test section, but at the same time, its pressure coefficient distribution should be as similar as possible to the one on a NACA6 airfoil (typical profile in turbomachine blades). It was found that attaching a NACA6 nose part to a flat box all these requirements were fulfilled and these are the reasons by which this arrangement was chosen as the experimental model. See Figure 9.

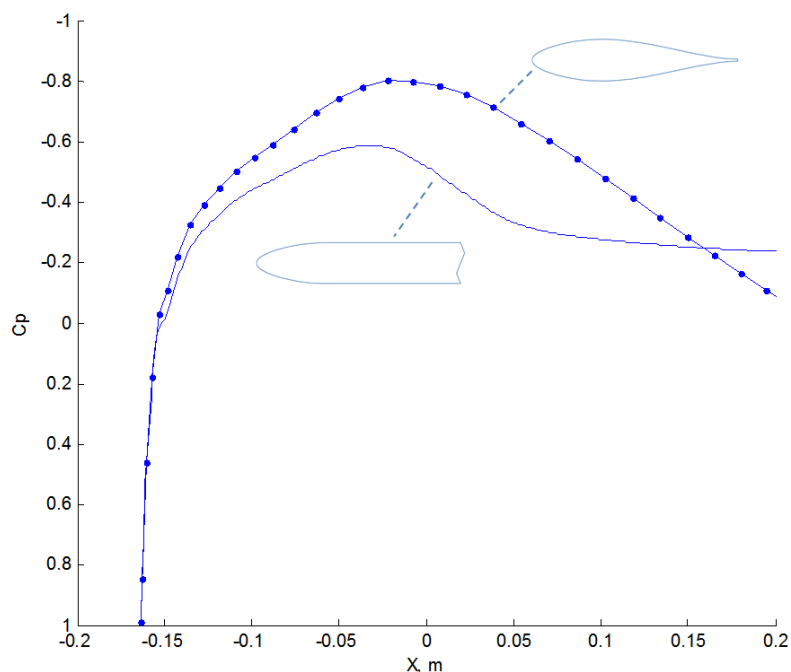


Figure 9: Comparison of pressure coefficient distribution on a NACA6 airfoil and on a model having NACA6 nose part attached to a flat box.

3.2 Experimental Set Up

Experiments were performed in a linear cascade facility at Chalmers University. Figure 10 shows the configuration of this facility, which is of open circuit blower type and operates at velocities up to 20 m/s. The cross section of the working part of the facility is 200 by 1200 mm. The test-facility consists of a wide-angle diffuser, a settling chamber with a honeycomb and grids, a contraction, and a test section. A 30 kW fan is used to drive the flow.

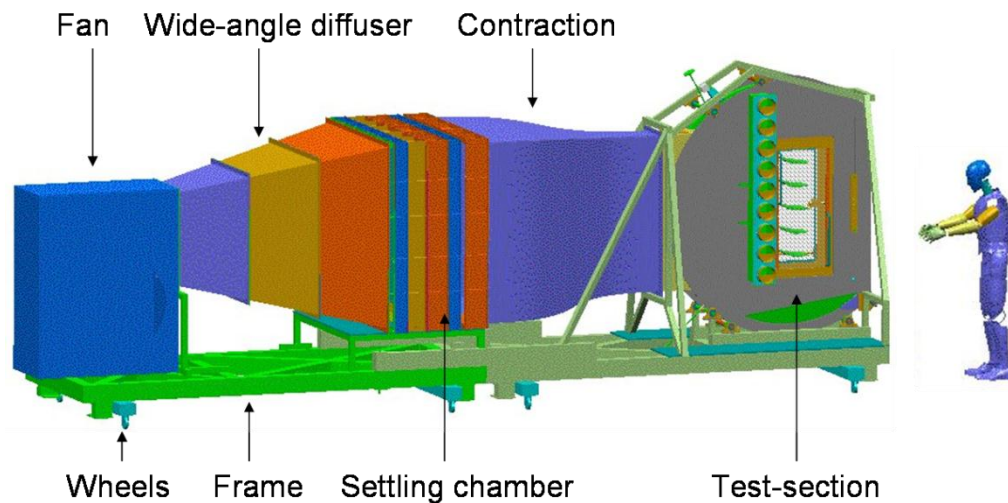


Figure 10: Test facility.

Figure 11 shows a sketch of the test section of the facility which is equipped with an end-wall boundary-layer suction system. Working flow incidence angles are designed to vary between 0 and 52 degrees relative to the axial inlet flow angle (for current experiments 0 degrees). A grid is used to create disturbances in the free stream and two turbulence intensities are procured for tests: 2% and 4%. For testing at 2% free stream turbulence intensity, the grid had to be placed at a distance “D” equal to 960 mm upstream from the point where $x=0$ (set up of coordinates explained later in this section). The grid then is moved so that $D=430$ mm, which is the distance needed to get 4% free-stream turbulence intensity. Different flow velocities (5, 9 and 18 m/s) are used and monitored using a Pitot-Prandtl tube connected to a digital micro-manometer, which also had sensors for temperature and absolute pressure readings.

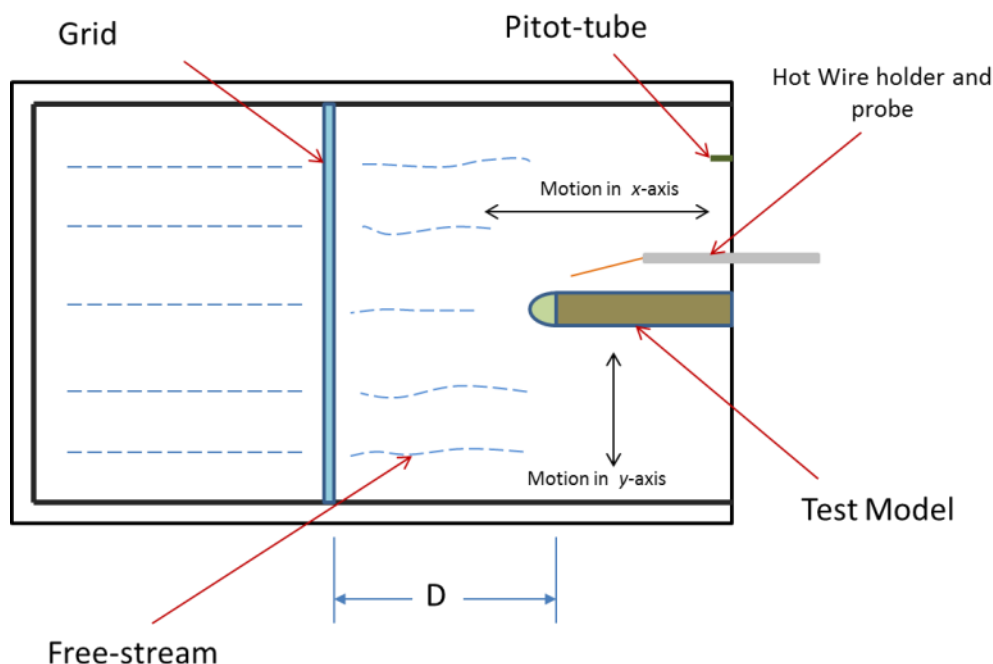


Figure 11: Sketch of the facility test section

The probe positioning is controlled by an automated traversing system. In these experiments, the inputs received by this system were x , y , z coordinates and therefore the motion was 3-dimensional and performed by means of stepper motors with a resolution of $1.6 \mu\text{m}$. For each case, the x was in the streamwise direction. The y was perpendicular (vertical) to x . Preliminary tests were performed to assure two-dimensionality and it was found that velocity profiles along the z (spanwise direction) were quite uniform. For that reason, the experiments were carried out keeping a constant z -coordinate. As mentioned before, 3 different speeds were used and as described and shown later, 4 different noses were manufactured, which means 12 cases in total for the same free stream turbulence intensity. For each of the 2% free stream turbulence intensity cases, 16 different points along x -axis were taken for measuring and for each x -point, 27 points along the y -axis were determined, for a total of 432 x , y , z coordinates or measuring points. Figure 12 shows schematically the measurement points. For clarity, the vertical distances of shown measurement domain are stretched about three times. The noses are attached to a flat box. Therefore, their curved surfaces get flat progressively. At the point where the noses are coupled to the box, the surface is no longer curved and gets completely flat and the x - y coordinates are set to be zero ($x = y = 0$). This means that the x -coordinates along the curved surface are negative and the x -coordinates along the flat box are positive. The $z=0$ (constant) is set by placing the probe in the middle of the spanwise length.

The CTA anemometer was equipped with a tungsten wire of 3 mm length and $5 \mu\text{m}$ in diameter. The probe calibration was performed in a dedicated calibrator and the results of the calibration are stored in a file. The maximum error in the probe calibration was within 0.5% for all calibration points.

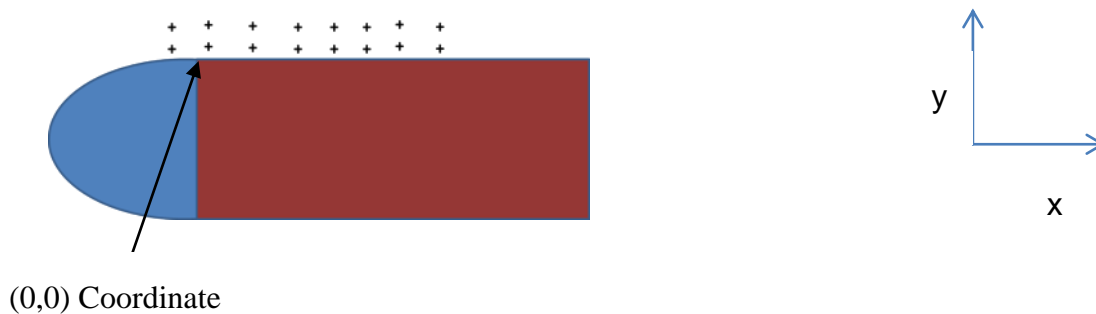


Figure 12: Illustrative sketch of typical measurement points over the complete model.

The noses used for the test models are manufactured using a stereo lithography technique which has a typical accuracy of $\pm 0.1\%$ of the model size. On Figure 13 a photo of three of the noses is shown. Models produced by this method have small traces on the surface due to a finite resolution of the machine. These traces were filled with epoxy coating and thereafter the surface was polished.



Figure 13: Noses used for the complete model.

For every nose, 15 small holes (1.7 mm diameter) were designed in order to place pressure taps to monitor the static pressure distributions. Those taps are connected to a 16-channel PSI 9116 digital pressure scanner (Pressure System Inc.) which has a measuring range of ± 2500 Pa. The accuracy of the scanner in the measurement range of current experiment (± 250 Pa) is ± 2 Pa. Figure 14 shows a section of the nose to see the holes used to monitor static pressures.



Figure 14: Section of one of the noses showing the holes for pressure measurements.

The experimental models were designed by using SolidWorks CAD software. The base configurations are two modifications of the NACA6 airfoil nose (a sharper modification and a more blunt modification). Two other models are created by changing the aspect ratio of the base configurations. The thickness-to-length ratio was decreased two times. Therefore, 4 different noses (for modeling of 4 different pressure gradients) were manufactured for testing. The resulting modified noses were named as

95N (large-scale sharp nose), 110N (large-scale blunt nose), 95sh (short version for 95N) and 110sh (short version for 110N). The flat part of the model is assembled by using plexi-glass plates and aluminum profiles.



Figure 15. Real model showing the box and nose assembly.

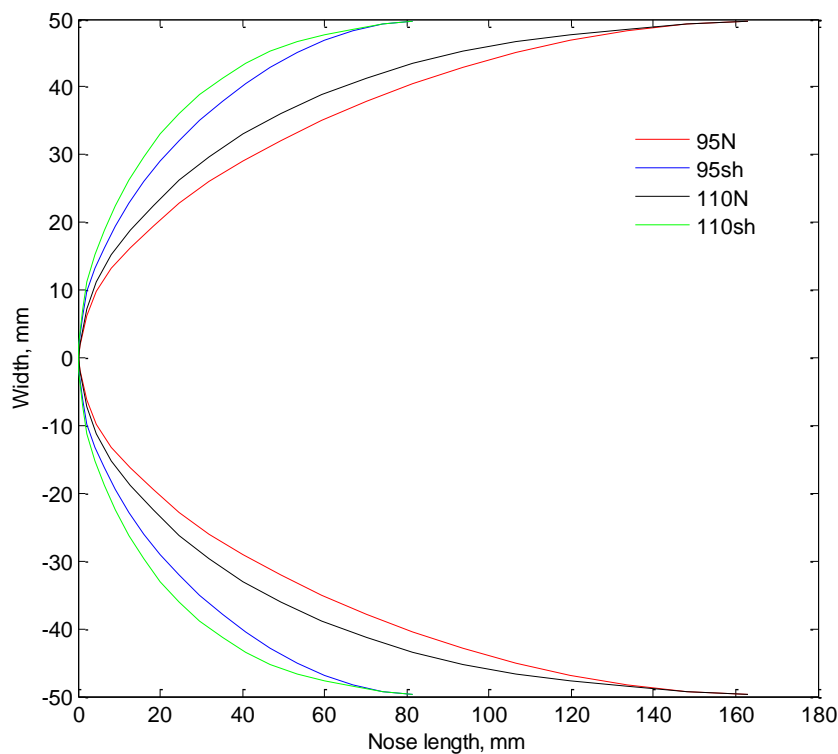


Figure 16. Differences in noses used for experiments

A smoothness of the attachment between the noses and the box was ensured by a specially designed adapter which was also manufactured by a stereo lithography. The adapter was carefully matched with the box and the noses to minimize any steps in geometry. Figure 15 illustrates the complete model and Figure 16 shows a comparison

of the different noses. More photos of the set up and the test facility are shown in the Appendix.

Probe positioning and data acquisition were fully automated and controlled by a PC with NI LabVIEW software. The software used for controlling motion is written using the LabVIEW graphical programming language, allowing the user to monitor current position, enter new coordinates and set speeds for each individual axis. Post processing of the experimental data was performed in Matlab (MathWorks Inc).

3.3 Data Processing Technique

The data was processed by using several written codes in Matlab (MathWorks Inc). At initial step the voltage data was converted to velocity with the help of a calibration file and major statistics is calculated, such as mean values and standard deviations. The resulting information was then stored for every case and contained values for Instantaneous velocities, Mean Velocities, The Root Mean Square of velocity fluctuations (RMS) and Static Pressures. Further processing included computation of the boundary layer parameters, filtering and spectral analysis of data which are explained in subsequent chapter.

CHAPTER 4

RESULTS

After processing the data, readable information ready for posterior usage were: Instantaneous velocities, RMS of velocity fluctuations, Mean velocities and Static Pressures.

4.1 Pressure Distribution

Different pressure gradients acting on the model boundary layers are obtained by implementing different geometry of noses. Pressure distributions for each of the four models are shown in Figure 17. The pressure distributions for both large-scale noses (95N and 110N) and their short versions (95sh and 110sh) are shown in terms of the pressure coefficient, C_p defined as in [23] versus $x-x_0$ (distance from leading edge). It is clearly seen that the 95-noses have the location of the pressure peak shifted downstream as compared to 110-noses and as a result the favorable pressure gradient extends up to the point of connection with the flat box. For the 110-noses the adverse pressure gradient starts already on the nose itself. The 110sh nose causes the strongest favorable pressure gradient and for three other noses the favorable pressure gradient strength is decreased in the following order: 95sh, 110N, 95N.

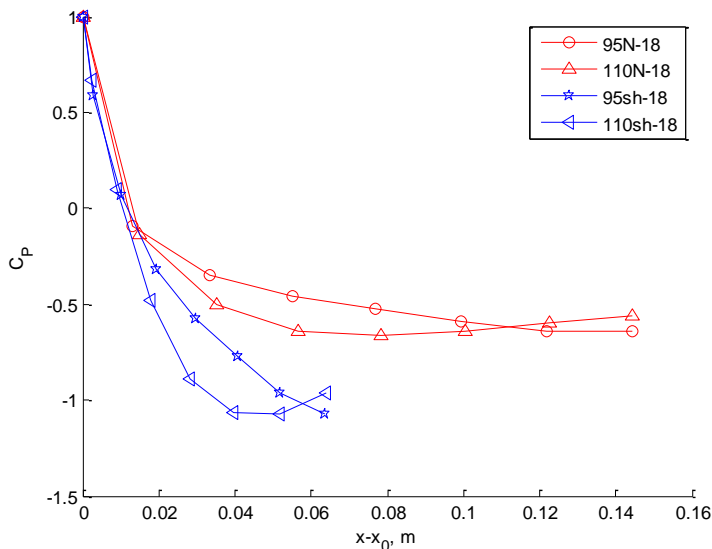


Figure 17: Static pressure distributions for the different models at 18m/s freestream velocity.

Since current models were not equipped with pressure taps in the area of adverse pressure gradient, to illustrate the adverse pressure gradient on the models, Figure 18 shows also distributions obtained from numerical calculations. The adverse pressure gradient is the strongest for the 95sh nose and the strength is decreased in the

following order: 110sh, 95N, 110N. In detail the CFD calculations will be discussed in one of subsequent sections.

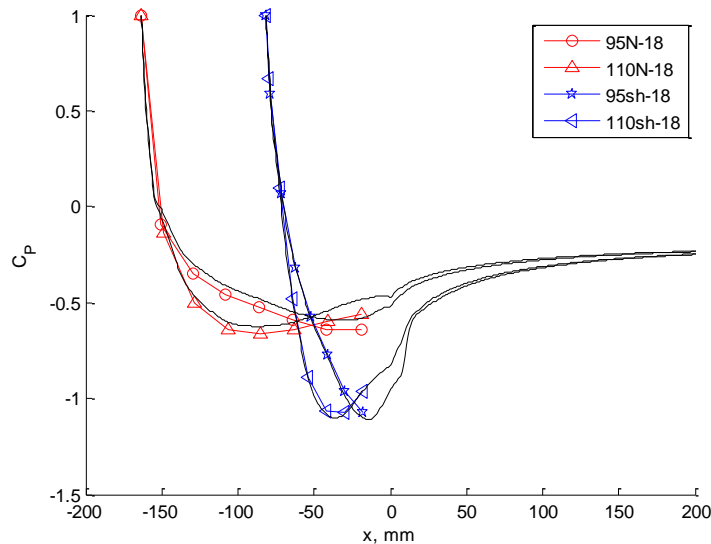


Figure 18: Static pressure distributions for the different models at 18m/s freestream velocity. Lines show corresponding numerical results.

4.2 Effect of Flow Reynolds Number

From the collected data it is possible to plot velocity and *rms* profiles for all cases. In Figure 19 it is possible to see the velocity profiles obtained for the 95N, 5 m/s and 2% free stream turbulence intensity case (mild favorable pressure gradient and low flow Reynolds number, Re) and profiles of *rms* of velocity fluctuations. From the mean velocity profiles plot it is possible to say that for the mentioned case, the flow starts behaving as laminar and not far from the Blasius profile¹. The Blasius solution can be seen depicted by a dashed line. Analysis of the profile shape factor, which will be given further, supports this fact as well. As we move downstream over the model, the flow changes gradually showing turbulent velocity profiles for the most downstream stations. The mean profiles for last two stations show noticeable similarity. The *rms* profiles at first stations show typical shape for laminar flow at high turbulence intensity [3]. With increased downstream position the intensity of fluctuations increases until reaching a maximum at $x=90$ mm. From this position the maximum of *rms* is shifted towards the wall which is typical for turbulent boundary layer. From the *rms* profiles it is clearly seen that the turbulence intensity in the freestream is about 2%. Although the profiles give clues regarding the behavior of the flow, boundary layer thickness and change from laminar to turbulent, they don't give clear quantitative information about where the transition is occurring.

¹ Solution of the boundary-layer equations for laminar flow with zero pressure gradient.

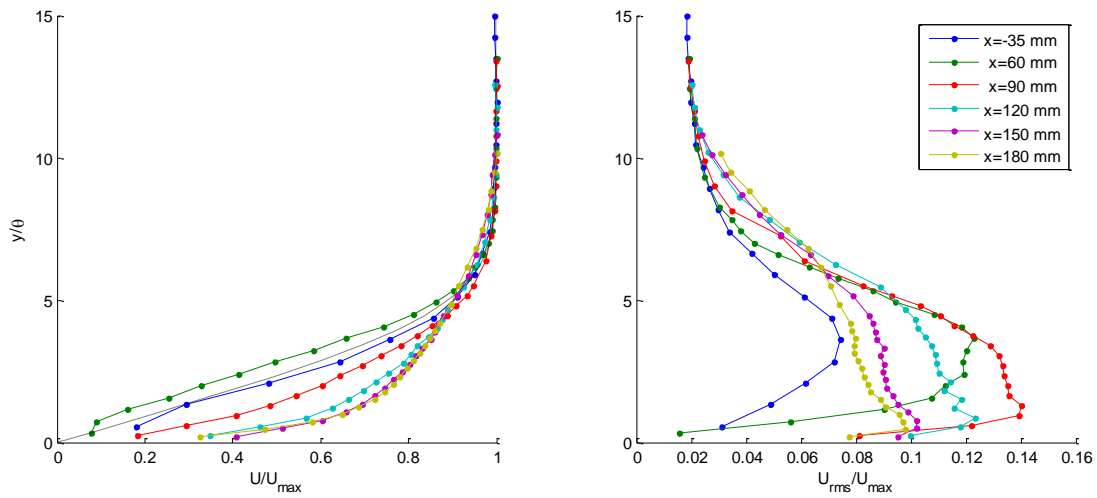


Figure 19: Velocity (left) and rms (right) profiles for nose 95N, 9m/s and freestream turbulence intensity, $Tu=2\%$

Contour plots of the mean velocities and the *rms* of velocity fluctuations were also obtained, to see more graphically the effects of different parameters on transition. Figure 20 shows a contour plot of the mean velocity. In this case, from the 95N nose at different Re . It is possible to see how the boundary layer is gradually becoming thinner and thinner as the local Reynolds number increases.

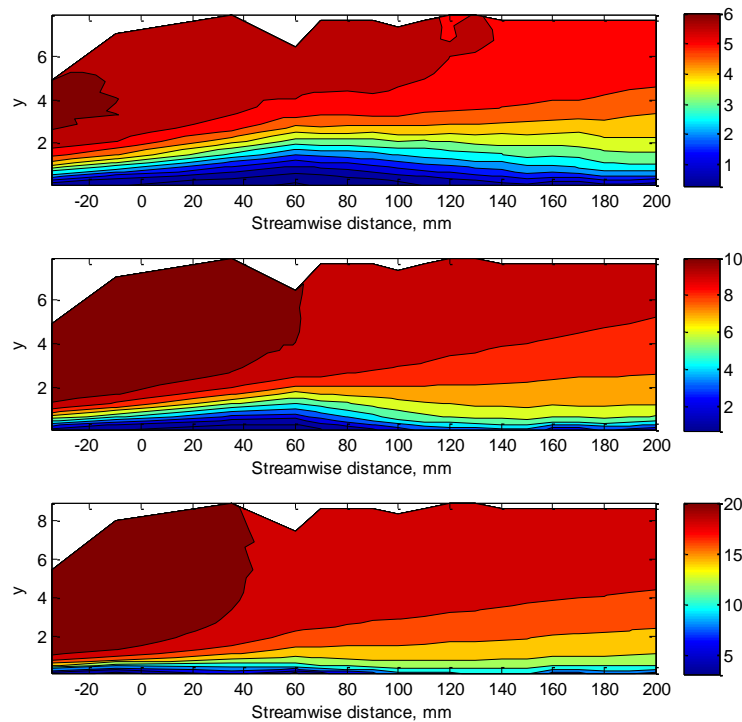


Figure 20: Contour of mean velocities for 95N nose. From top to bottom 5, 9 and 18 m/s.

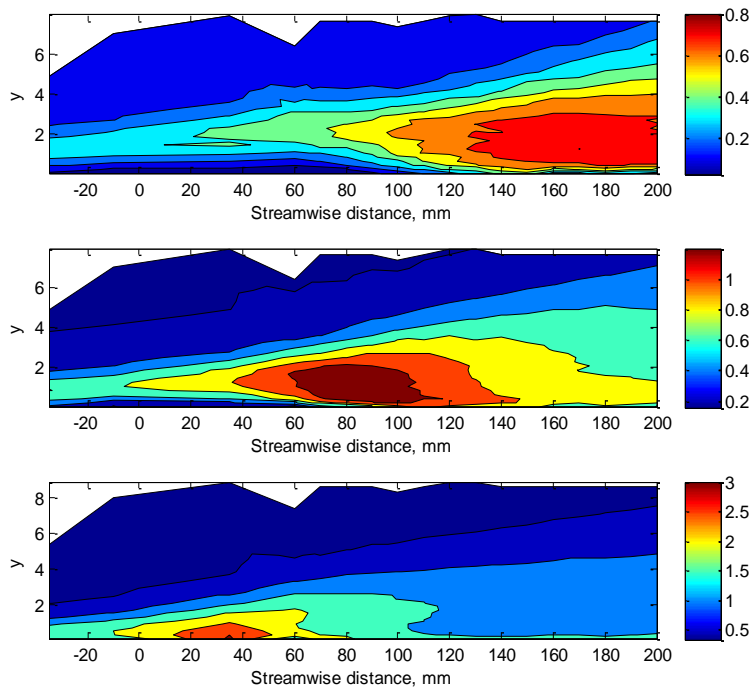


Figure 21: rms contour plots for different Re and nose 95N. From top to bottom 5, 9 and 18 m/s

From contour plots in Figure 21, drawn for the same cases, it is clearly visible how a turbulent region moves upstream as Re increases. It also shows that rms amplitude is higher when Re is higher. The relative amplitude of rms fluctuations is however same in all cases, around 15%, as seen from Figure 22.

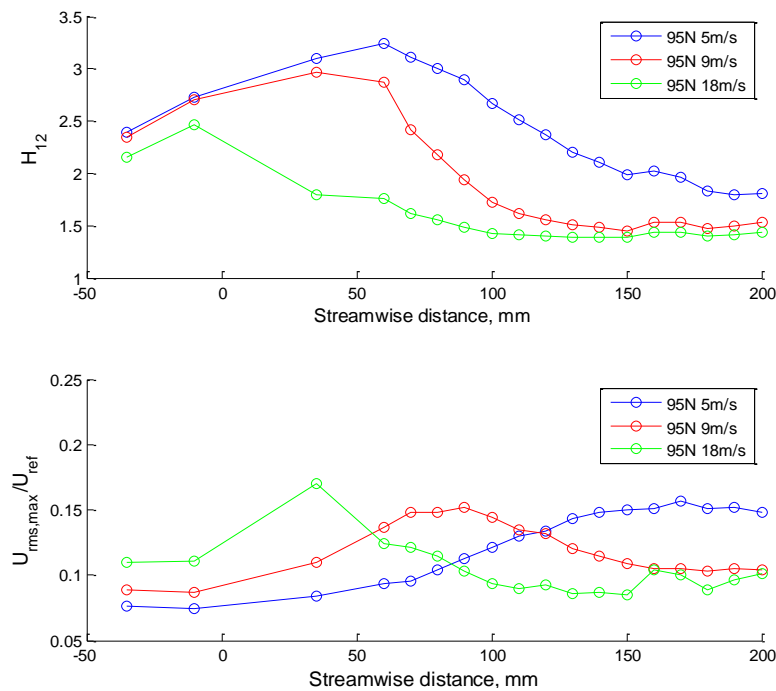


Figure 22: Shape factor and rms plots (top and bottom respectively) for different Re , using nose 95N and $Tu=2\%$

According to Abu-Ghannan and Shaw [8], transition can be expressed in terms of Reynolds number based on the momentum thickness and the shape factor. For a certain flow condition, their paper shows that the transition onset is at the point where the shape factor starts decreasing. It is well-known [24] that for the Blasius boundary layer the shape factor is 2.59, for a boundary layer at the limit of separation the shape factor is 3.85 and for a turbulent boundary layer on a flat plate the shape factor is 1.3. Figure 22 shows two plots: the variation of the shape factor (H_{12}) and the *rms* of velocity fluctuations along the streamwise distance for the same cases mentioned previously (with nose 95N, different Re and $Tu=2\%$). Keeping in mind the experimental set up, the negative values for the streamwise distances in the plot correspond to the points along the nose of the model (curved surface). From 0 (zero) on, the distances indicate those positions along the flat surface. From Figure 22 one can observe that the shape factor at $x=-20$ mm where the pressure gradient is zero is indeed very close to the value for Blasius boundary layer. At stations downstream, in adverse pressure gradient, the shape factor is increasing while is staying below the separation value of 3.85. At the most downstream positions the shape factor is approaching value of 1.5 which is a typical value for a turbulent boundary layer. As can be seen from the plot, a drop in the shape factor for low and medium Re occurs more downstream than for the case at high Re (for 5 m/s this is occurring at around +70 mm, for 9 m/s occurring at around +40mm and at around -15 mm for 18 m/s). Moreover, the highest shape factor is obtained for the lowest Re case, indicating that for this case, the risk of flow separation is the highest [16].

On the other hand, the *rms* plot of velocity fluctuations show peaks at different streamwise distances (for every case) which correspond to those points on the shape factor plot where the shape factor starts to decay. The points at which the velocity fluctuations has reached maximum values indicate those where it is possible to find turbulence and indicates the end of the transition region. As it will be shown later this point correlates with the point of 75% intermittency. A more strict definition of the transition end assumes that a fully developed turbulent boundary layer is formed which happens as the shape factor approaching value of 1.5. Finally, it is possible to note that the lowest Re produces the longest transitional region.

4.3 Effect of Pressure Gradient

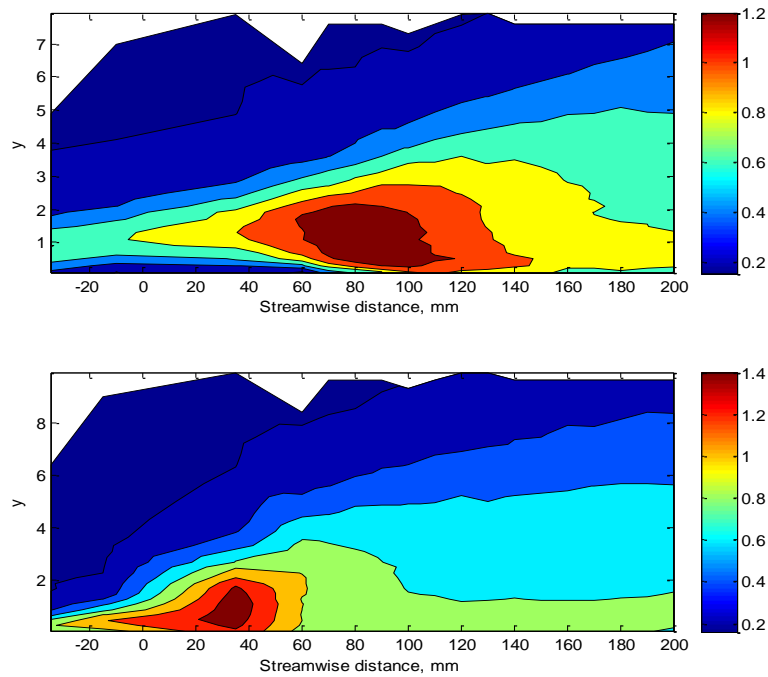


Figure 23: Turbulence promotion for different pressure gradient (95N top and 110sh bottom). Same Re (at 9 m/s) and Tu (2%).

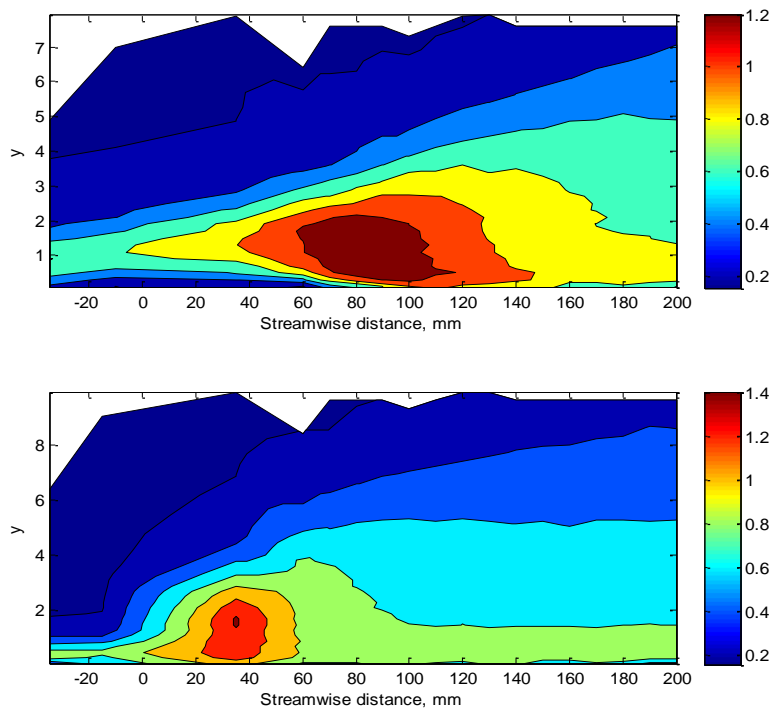


Figure 24: Turbulence promotion for different pressure gradients (95N top and 95sh bottom). Same Re (at 9 m/s) and Tu (2%).

The contour plots in Figure 23 show turbulence moving upstream when a stronger adverse pressure gradient is present. The level of maximum turbulence is also higher in that case, when compared to less strong adverse gradient case. Turbulence promotion is also observed in Figure 24, when the boundary layer is subjected to the strongest adverse pressure gradient. In Figure 25 the onset of transition is visualized in terms of shape factor and *rms*. At the same speed and free-stream turbulence level, the effect of increased adverse pressure gradient is, as might be expected, an earlier transition start (start of shape factor decay). The *rms* plot in same figure shows the peaks indicating the end of transition. By looking at the points where the transition starts and finishes, it is seen that the length of the transitional region is also decreased in case of stronger adverse pressure gradient from 100 mm to 50 mm.

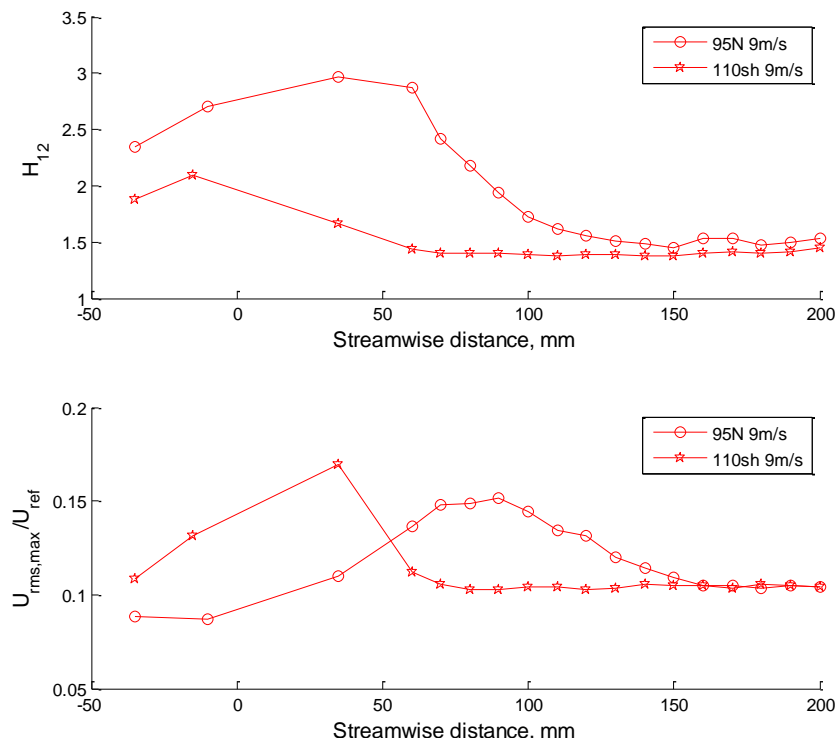


Figure 25: Shape factor and RMS plots (top and bottom respectively) for same Re and Tu , but different pressure gradients.

In Figure 26 a comparison of the effects caused by different local Reynolds numbers and pressure gradients is shown. From this plot is possible to observe that at stronger adverse pressure gradients the shape factor variation with changing of flow velocity is decreased.

The effect of pressure gradients on Reynolds number based on the momentum thickness Re_θ is shown in Figure 27. By observing the negative streamwise distances (from -50 to 0), it is easily inferred that Re_θ increases as the nose of the model is elongated. It is noticeable that for short 110sh-nose Re_θ has nearly same values in the favorable gradient, at $x = -35$ for different velocities. As soon as the pressure gradient becomes adverse, the effect on Re_θ is greater and together with the flow velocity variation, the impact on Re_θ is much more noticeable.

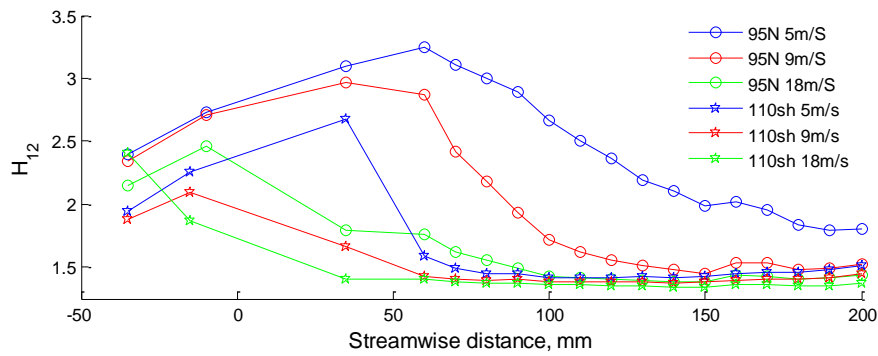


Figure 26: Comparison: Shape factors for different Re and pressure gradients.

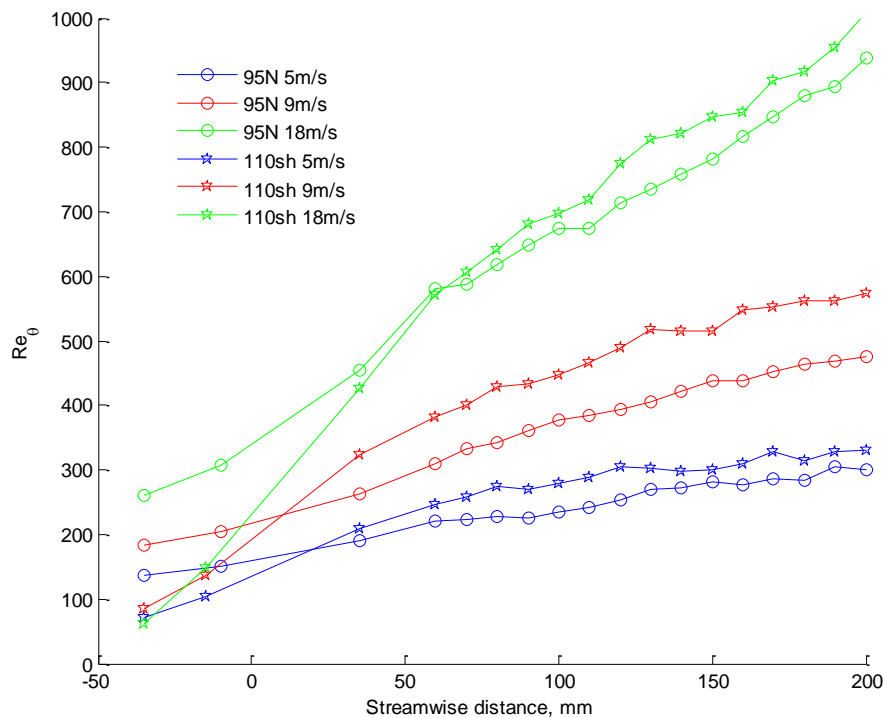


Figure 27: Reynolds number momentum thickness for same Tu , different speeds and pressure gradients

4.4 Effect of Free-stream Turbulence Intensity

The plot in Figure 28 shows graphically how boundary layer turbulence varies when the free-stream Tu is different. As it is expected, higher Tu promotes the transition onset. Figure 29 shows the shape factor plot which confirms an earlier decay when increasing Tu . This plot also shows that for the same Re , the shape factor seems to be more sensitive to free-stream turbulence effects, but for mild and higher Re , both the flow velocity and the free-stream turbulence level have almost the same effect on the shape factor values and therefore, on transition inception. The *rms* peaks show that the length of the transitional region seems to decrease as Tu is higher. Noticeable that in

the case of $Tu=4\%$ and highest velocity the transition occurs already in the zone of favorable pressure gradient.

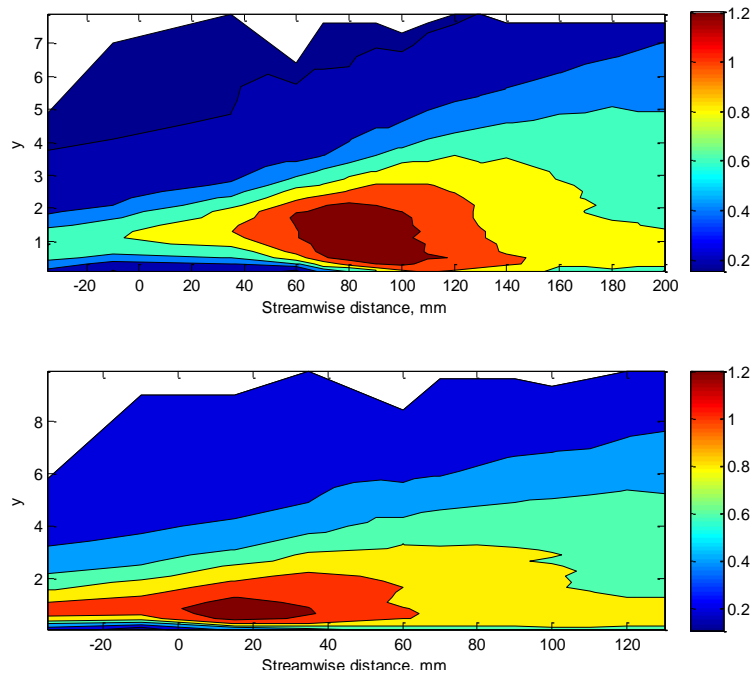


Figure 28: RMS contour plots for different Tu (2% on top and 4% at bottom). Same Re (at 9 m/s) and pressure gradient

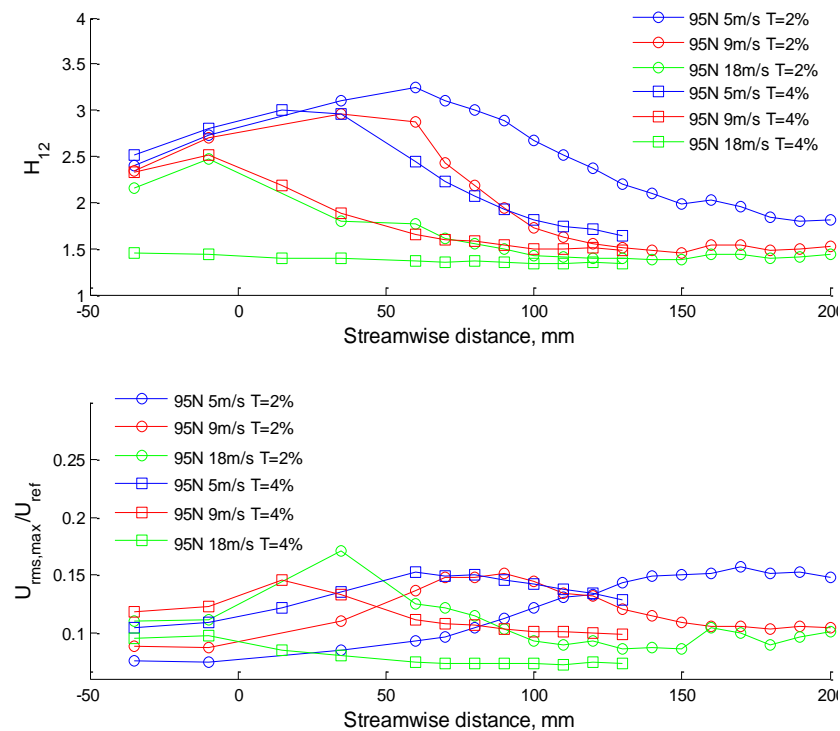


Figure 29: Shape factor and RMS of velocity fluctuations (top and bottom respectively) influenced by free-stream turbulence intensity.

The next plot (Figure 30) shows that the pressure gradient effects have about same influence on the shape factor values as the effect caused by changing Tu for the same

Re. It is noticeable that the peak value of the shape factor for a shorter nose is lower than the peak obtained for the longer nose with higher *Tu*. Moreover, the shape factor decay moves more upstream for the former case.

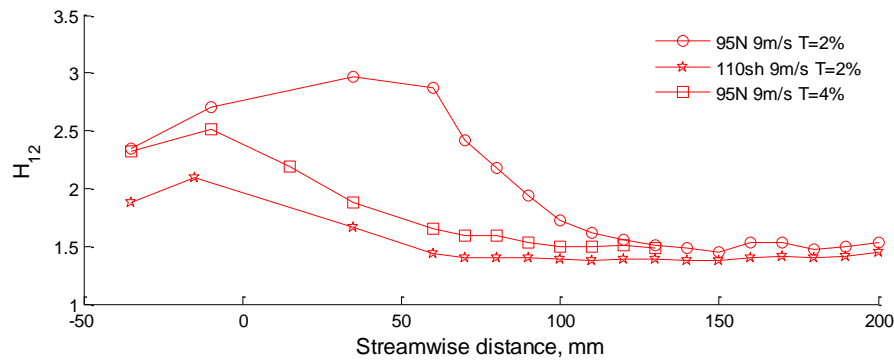


Figure 30: Comparison: effect of pressure gradient and *Tu* on shape factors at 9m/s.

Figure 31 shows the effect of free-stream turbulence intensity on Re_{θ} . At constant mild favorable pressure gradients, higher flow velocities together with higher free-stream turbulence intensity causes an increase in the Reynolds number momentum thickness. At low velocity, the free-stream turbulence intensity has about the same effect as the flow Reynolds number on Re_{θ} . As the streamwise distance increased, the effect of the turbulence intensity of the free-stream on Re_{θ} becomes more pronounced.

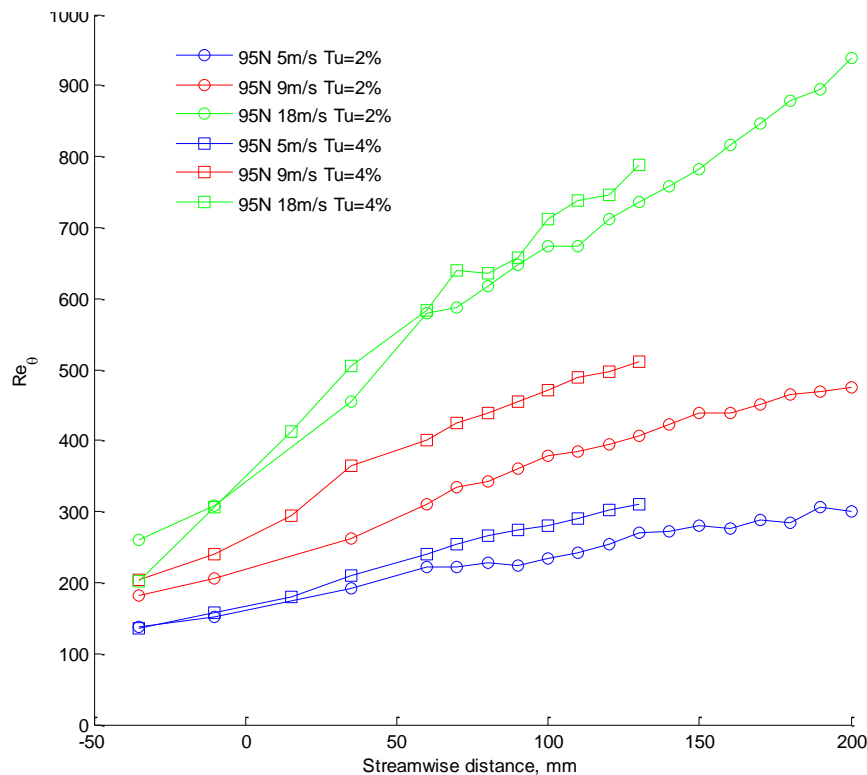


Figure 31: Reynolds number momentum thickness at different free-stream turbulence intensity and pressure gradients.

4.5 Filtered RMS

Figure 32 shows a typical instantaneous velocity signal from the tests. From this signal it is possible to see that as we move downstream, the traces get more and more chaotic and with higher frequencies. Those high frequency traces indicate the presence of burst or turbulent regions in the flow. In order to identify the place where these high frequency regions within the flow are taking place, it is necessary to filter out low frequency signals.

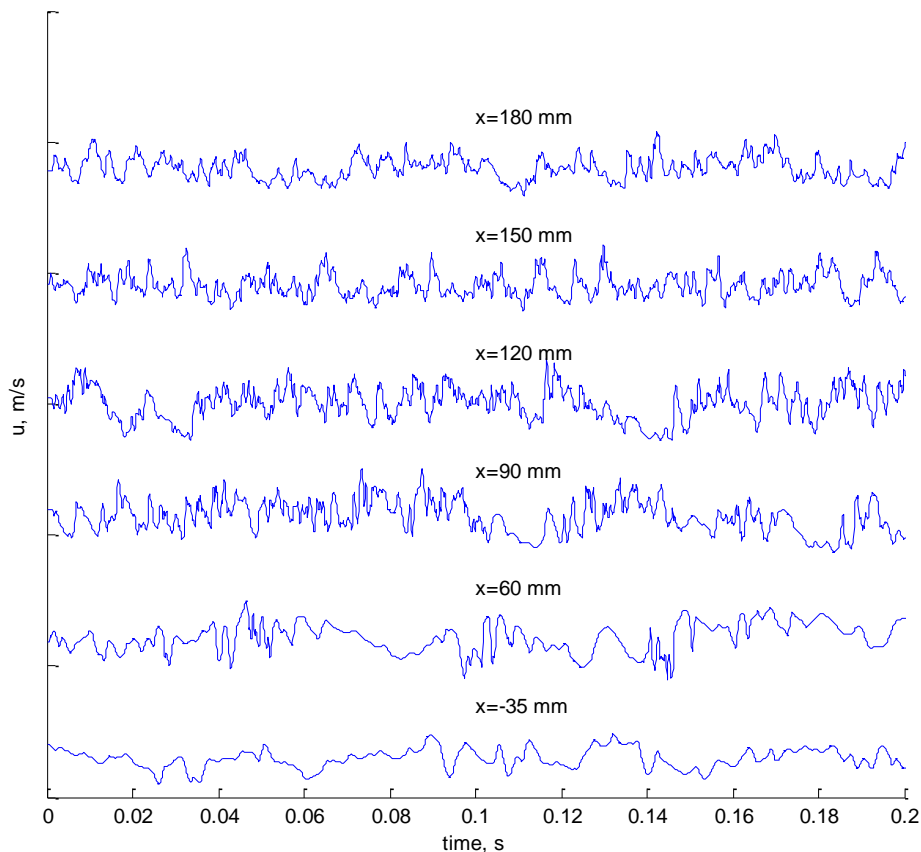


Figure 32: Typical instantaneous velocity signal. Case 95N, velocity 9 m/s.

The high-pass filtering was performed to remove frequencies which correspond to the wavelengths, $\lambda = U_{in}/f$ which are larger than 10 mm ($\sim 5\delta$). After high-pass filtering the data to take out the low frequencies, the *rms* of fluctuations for the remaining data was graphically shown by means of contour plots. The resulting contours are shown in Figure 33. From these plots, it can be seen that the transition onset occurs when the contours change its color from dark blue. These plots show how the transition onset behaves as the local Reynolds number, pressure gradient and turbulence intensity change.

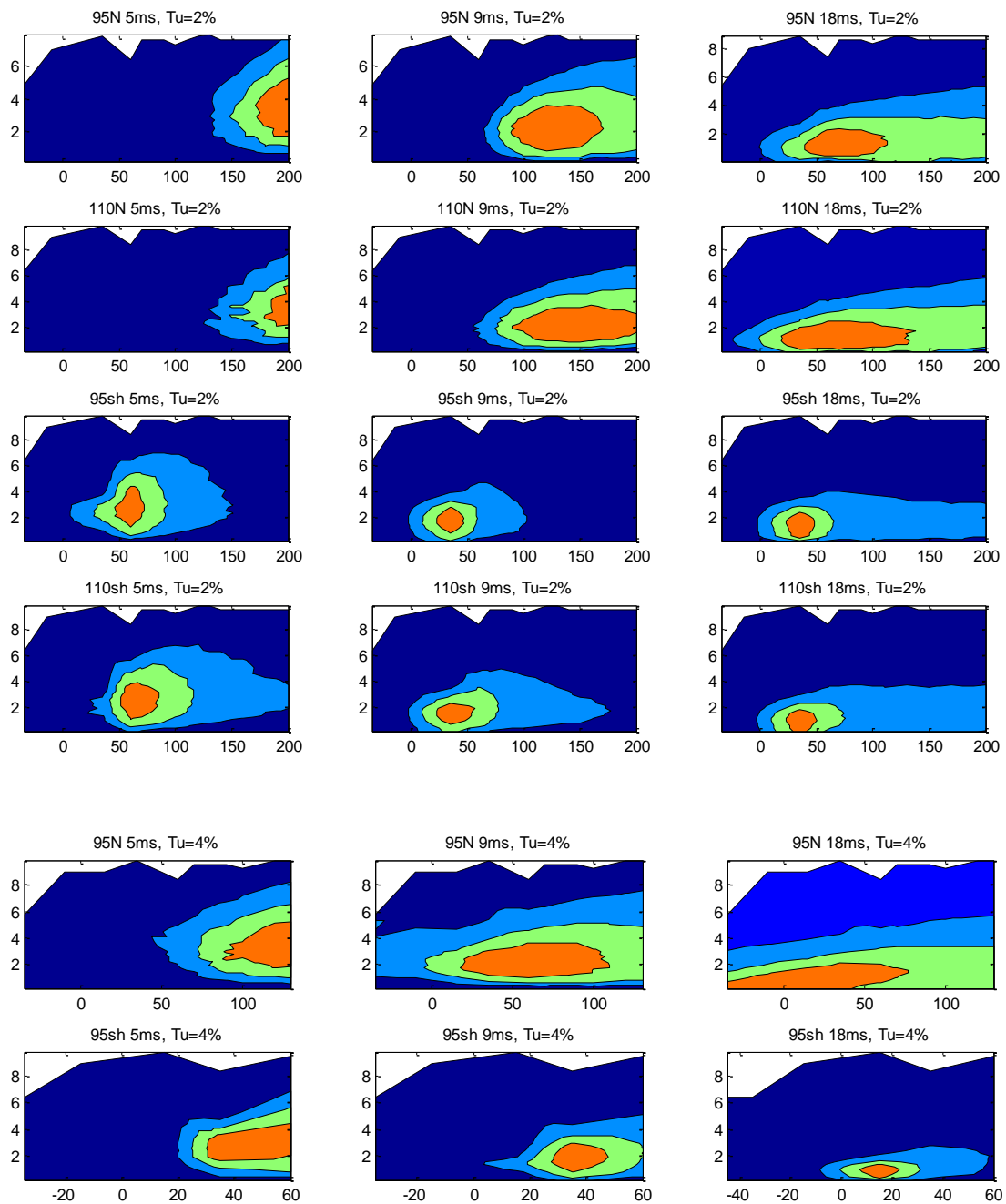


Figure 33: Filtered rms contours for different speed, pressure gradient and free-stream turbulence cases. Contour levels are 0, 0.25, 0.5 and 0.75 of the maximum amplitude.

The intermittency within the flow was also calculated for one of the cases and shown in Figure 34. This figure shows how it varies when calculated at different streamwise positions. At $x=150$ mm is noticeable that the intermittency value is equal to unity, indicating that at this position the flow is fully turbulent. At $x=180$ mm however, variation from 0 to 1 in the intermittency values is found, indicating transition (specifically reverse transition), caused by a relaminarization of the flow. Figure 35

shows the contours of intermittency and the streamwise positions at which intermittency values are no longer zero (0) and the flow starts being transitional.

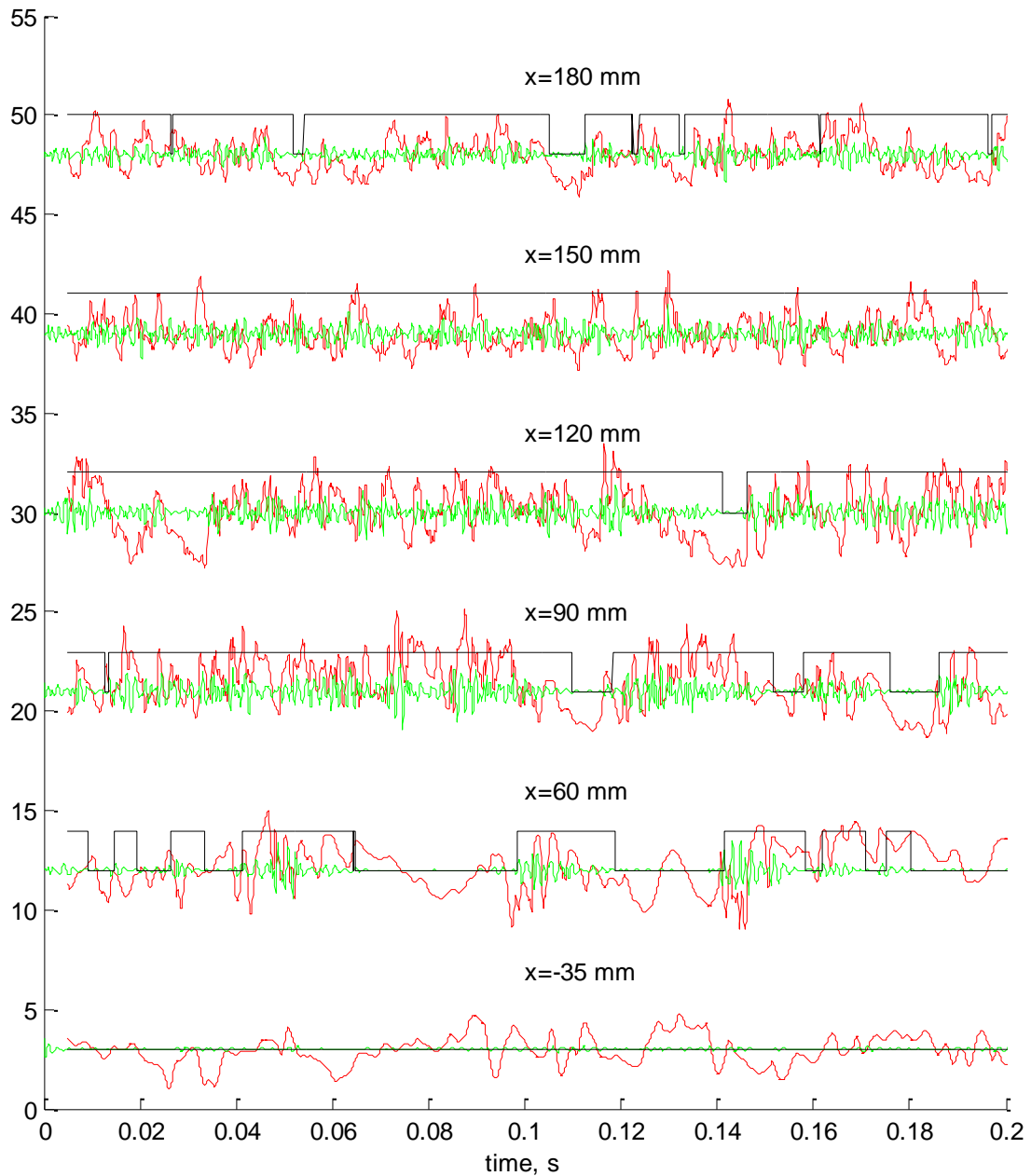


Figure 34: Illustration of finding intermittency. Different lines depict: instantaneous velocity signal (red), high-pass filtered signal (green) and intermittency function (black). Case 95N, velocity 9 m/s.

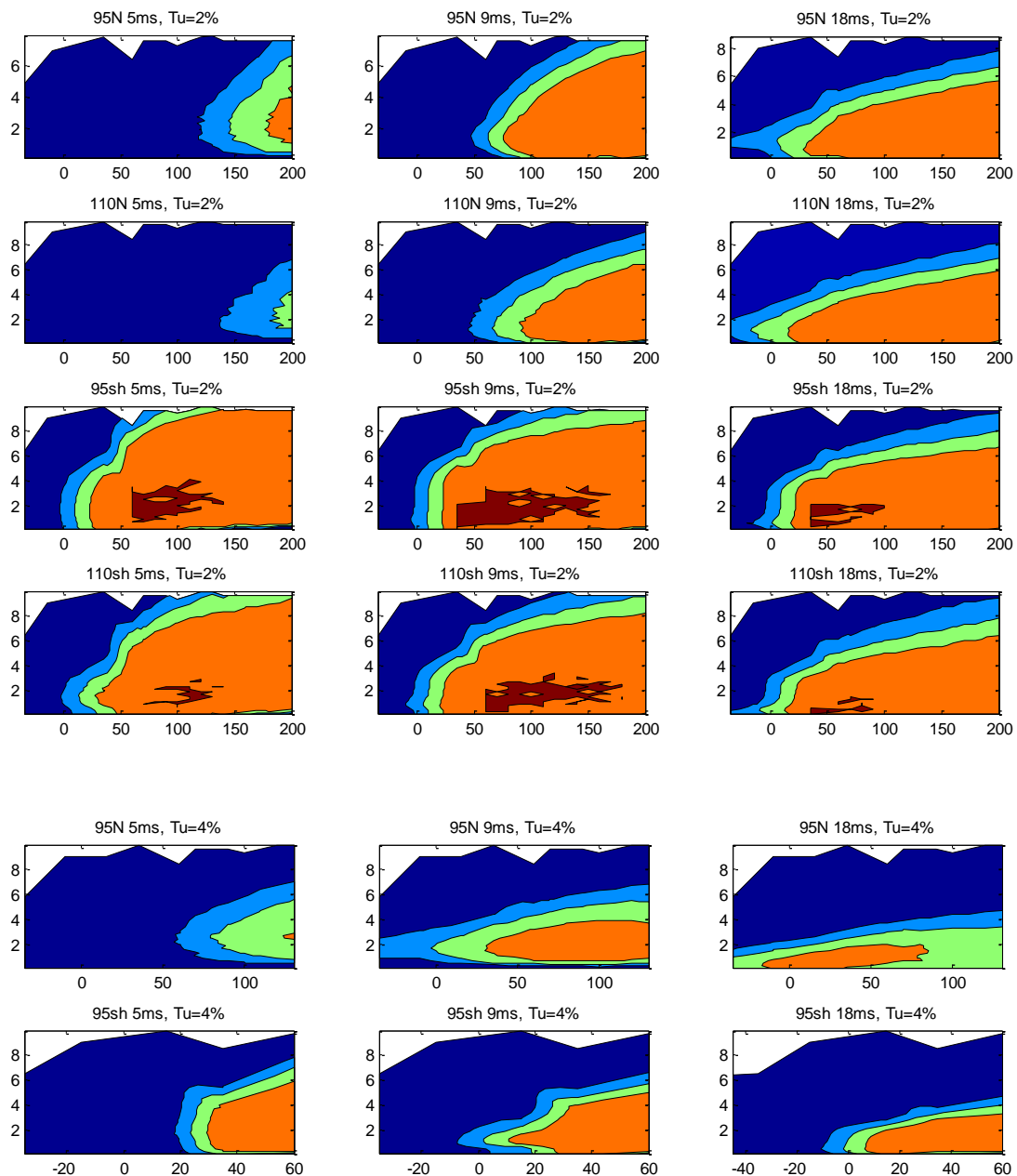


Figure 35: Intermittency contours for different speed, pressure gradient and free-stream turbulence cases. Contour levels are 0, 0.25, 0.5, 0.75 and 1.

4.6 Comparison of CFD Calculations and Experiments

It is well known that the simulation of laminar-turbulent transition is particularly challenging task for turbulence modeling. A number of turbulence models are developed which claim possibility of transition prediction and none of them is proven to be flawless so far. A relatively new transition model suggested by Langtry and Menter [25] was used in current study by means of ANSYS Fluent software. These numerical calculations were performed for same geometries as in experiments and

were validated by using current experiments. The two-dimensional computations were performed. Structured computational meshes consist of 10^5 quadrilateral cells with an O-grid and resolved boundary layers surrounding the model. Pressure based implicit finite volume solver was used, and the discretization schemes were second-order accurate. Calculations were performed with constant air properties. Boundary conditions in numerical calculations are matched with experimental conditions in the wind tunnel. At the inlet the velocity, turbulence intensity and inlet turbulent length scale are set as in experiments.

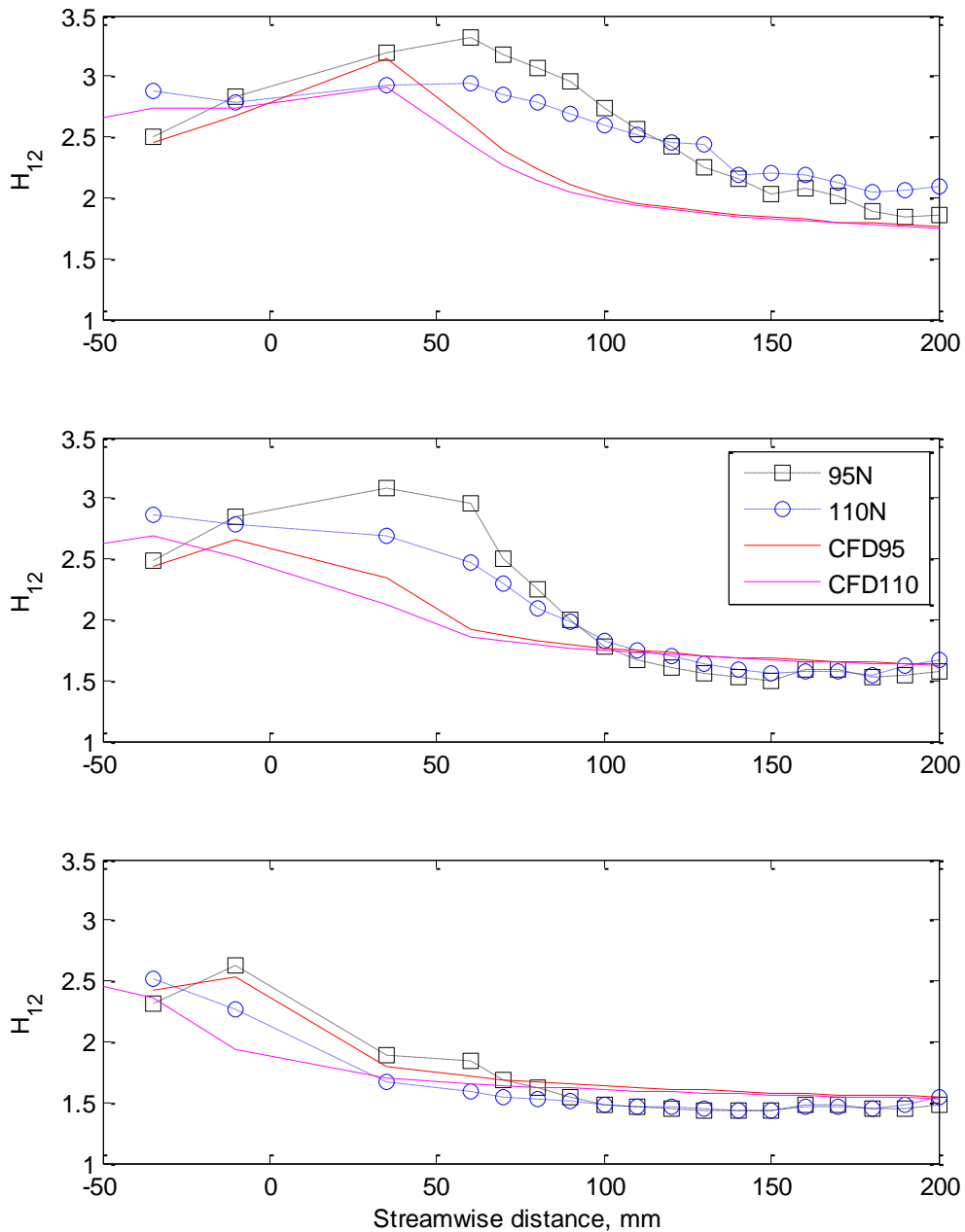


Figure 36: Comparison of CFD (lines) and experiments (symbols) for noses 95N and 110N at 5m/s, 9m/s and 18m/s (from top to bottom) and $Tu=2\%$.

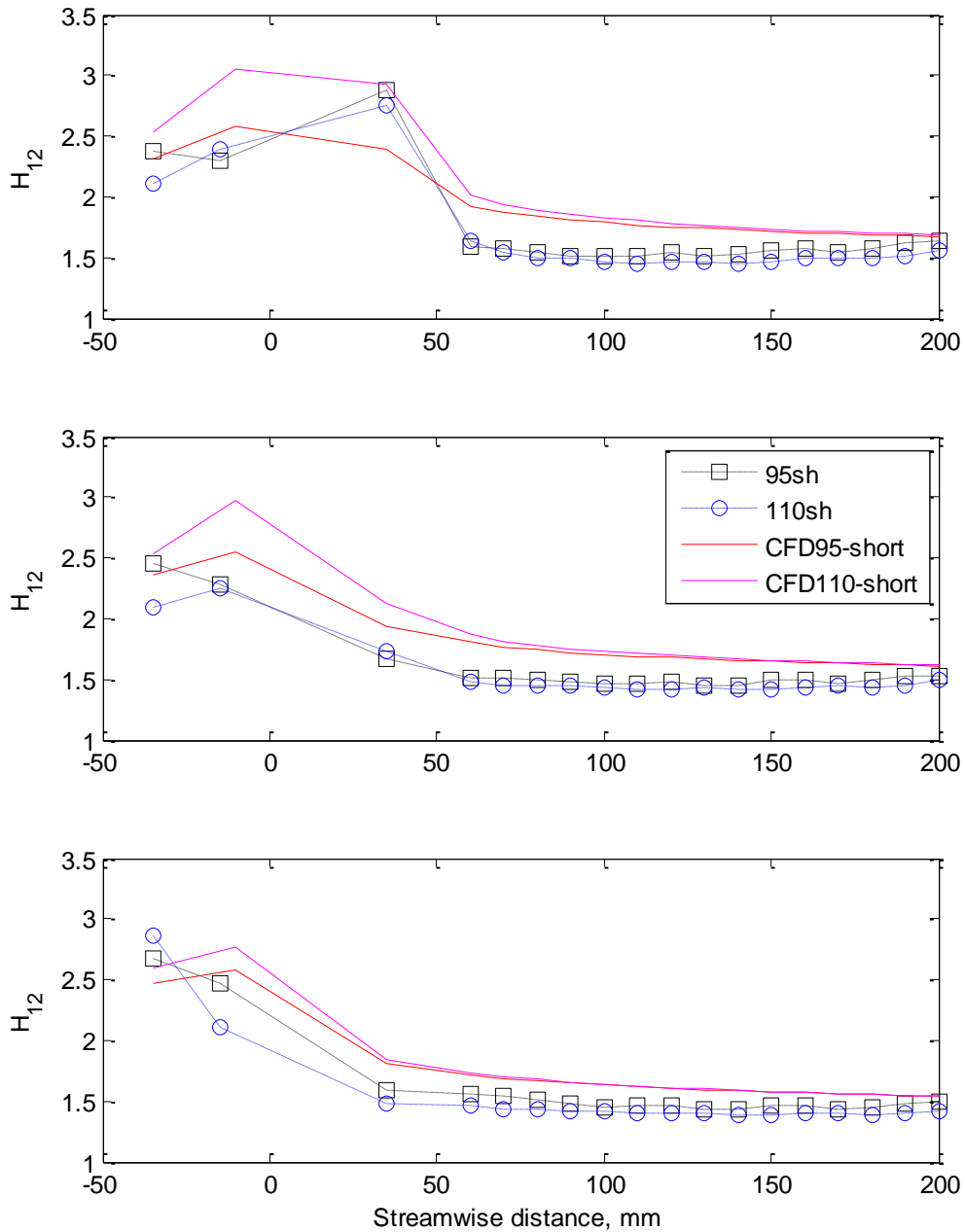


Figure 37: Comparison of CFD (lines) and experiments (symbols) for noses 95sh and 110sh at 5m/s, 9m/s and 18m/s (from top to bottom) and $Tu=2\%$.

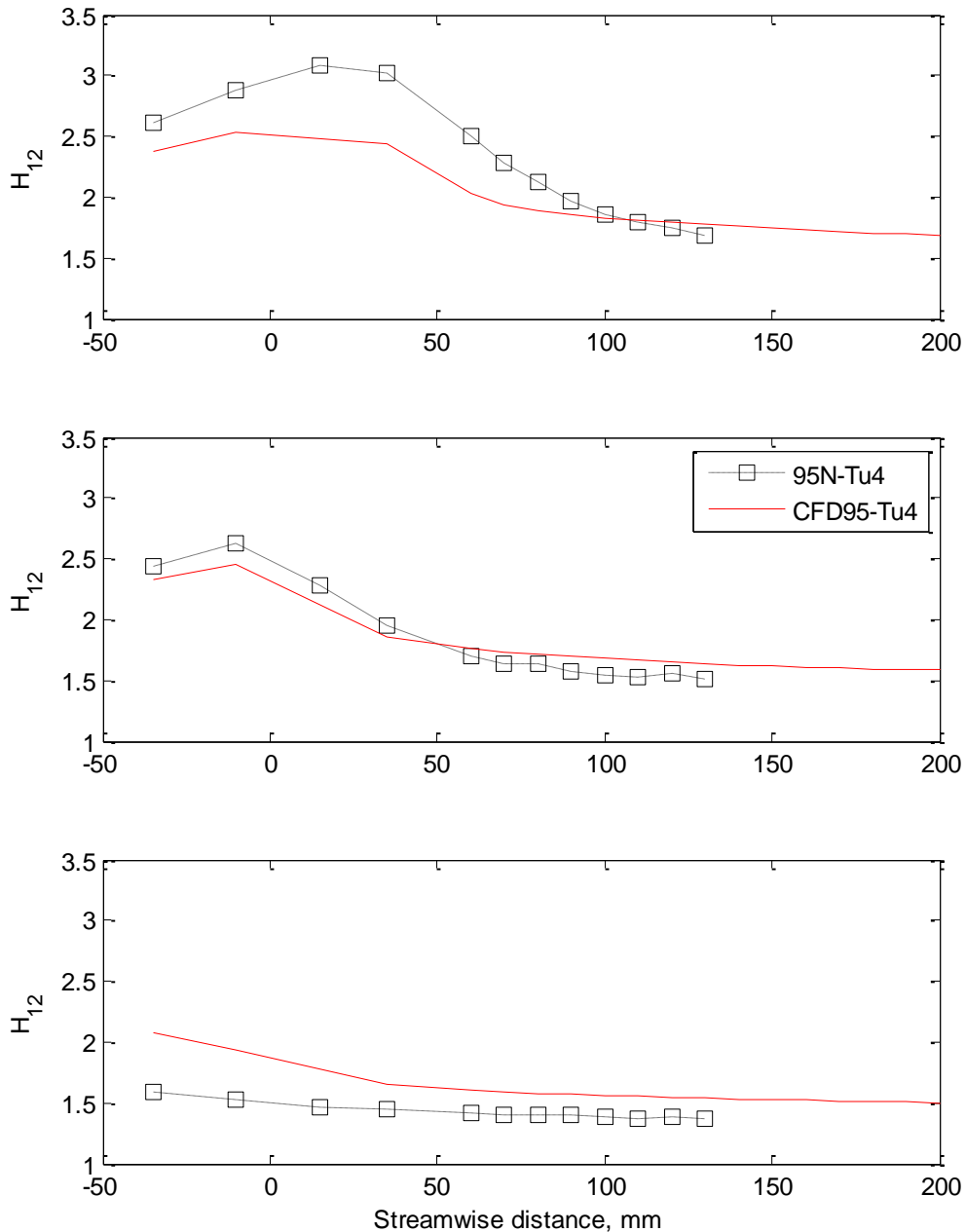


Figure 38: Comparison of CFD (lines) and experiments (symbols) for nose 95N at 5m/s, 9m/s and 18m/s (from top to bottom) and $Tu=4\%$.

Figures 36 to 38 show relevant results when CFD and experiments are compared. It is possible to see that for mild adverse pressure gradient, the predictions are quite good at high flow velocities (Figure 36). Rather good predictions are observed at all flow velocities and strong adverse pressure gradient (Figure 37). When the turbulence intensity is increased, the mid flow velocity and mild adverse pressure gradient case showed the best result (Figure 38). For $Tu=4\%$ and velocity of 9 m/s the transition occurs already in the zone of favorable pressure gradient. In this case the CFD is under predicting the transition. In general the CFD tends to over predict transition at mild adverse pressure gradients and at strong adverse pressure gradient.

CONCLUSIONS

Laminar-turbulent transition at high free-stream turbulence in boundary layers of the airfoil-like geometries with presence of the external pressure gradient changeover has been studied experimentally. This study will help deepen our understanding of the transition phenomena especially for engineering applications.

The experimental data were collected for a number of flow cases with different flow Reynolds number, turbulence intensity and pressure gradient distributions. The flow parameters selected are typical for turbomachinery applications and many other engineering applications. A database for further studies and validation of numerical calculation is one of the major benefits.

The results from experiments show that the transition onset is promoted when the flow Reynolds numbers and the free-stream turbulence intensity are increased. This happened even when the boundary layers are subjected to strong favorable pressure gradients and adverse pressure gradients.

Preliminary numerical calculations for same geometries and flow conditions as in experiments by using SST model with transition by Langtry and Menter were tested. CFD shows rather good prediction of transition location for cases with strong adverse pressure gradient for both studied turbulence levels. In cases of mild adverse pressure gradient CFD computations demonstrate a satisfactory prediction with some over-prediction of the transition onset. In opposite, the transition is under-predicted for case of transition start in zone of favorable pressure gradient.

In order to validate further performance of numerical tools for transition modeling, more studies involving the measurements and computations of heat transfer are suggested for future work.

REFERENCES

- [1] L.U. Schrader, L. Brandt, C. Mavriplis and D.S. Henningson: "Receptivity to free-stream vorticity of flow past a flat plate with elliptic leading edge" *J. Fluid Mechanics* 653, p. 245-271
- [2] W.S. Saric, E.B. White and H.L. Reed: "Boundary layer receptivity to freestream disturbances and its role in transition" 30th AIAA Fluid Dynamics Conference, AIAA-99-3788, p. 1-18, 1999.
- [3] S.V. Zhigulev, A.A. Uspenskii and M.V. Ustinov: "Effect of the Freestream Turbulence Scale and the Leading Edge Shape on Boundary Layer Laminar-Turbulent Transition" *Fluid Dynamics* 44, p. 31-44.
- [4] R.W. Radomsky, K.A. Thole: "Flowfield Measurements for a Highly Turbulent Flow in a Stator Vane Passage", *ASME Journal of Turbomachinery* 122, p. 255-262, 2000.
- [5] R.W. Radomsky, K.A. Thole: "Detailed Boundary Layer Measurements on a Turbine Stator Vane at Elevated Freestream Turbulence Levels", *ASME Journal of Turbomachinery* 124, p. 107-118, 2002.
- [6] S. Corrsin: "Investigation of flow in an axially symmetrical heated jet or air". NACA, Wartime Report, W-94, 1943.
- [7] L.S.G. Kovasznay, V. Kibens and R.F. Blackwelder, *J. Fluid Mechanics* 41, p.283, 1970.
- [8] B.J. Abu-Ghannam, R. Shaw: "Natural Transition of Boundary Layers-The Effects of Turbulence, Pressure Gradient, and Flow History", *IMEchE Journal Mechanical Engineering Science* 22, p. 213-228, 1980.
- [9] J.P. Gostelow, A.R. Blunden and G.J. Walker: "Effects of Freestream Turbulence and Adverse Pressure Gradients on Boundary-Layer Transition", *ASME Journal of Turbomachinery*, 116, p. 392-404, 1994.
- [10] G.J. Walker, J.P. Gostelow: "Effects of Adverse Pressure Gradients on the Nature and Length of Boundary-Layer Transition", *ASME Journal of Turbomachinery*, 112, p. 196-205, 1990.
- [11] W.J. Solomon, G.J. Walker and J.P. Gostelow: "Transition Length Prediction for Flows with Rapidly Changing Pressure Gradients", *ASME Journal of Turbomachinery*, 118, p. 744-751, 1996.
- [12] Mark W. Johnson, Ali H. Ercan: "A physical Model for bypass transition", *International Journal of Heat and Fluid Flow*, 20, p. 95-104, 1999.

- [13] R.E. Mayle: “The 1991 IGTI Scholar Lecture: The Role of Laminar-Turbulent Transition in Gas Turbine Engines”, ASME Journal of Turbomachinery 113, p. 509-537, October 1991.
- [14] F. Bario, C. Beral: Boundary layer measurements on the pressure and suction sides of a turbine inlet guide vane”, Experimental Thermal and Fluid Science 17, p. 1-9, 1998.
- [15] K. W. Van Treuren, T. Simon, M. Von Koller, A. R. Byerley, J. W. Baughn, R. Rivir,: “ Measurements in a turbine cascade flow under ultra-low Reynolds number conditions” ASME Journal of Turbomachinery , 124 p. 100-106, 2002.
- [16] Web site: http://www.cortana.com/Drag_Description.htm
- [17] Web site: <http://www.aeroflight.com/papers/bl/node2.html>
- [18] Frank M. White: “Fluid Mechanics” McGraw Hill, United States of America, 1994, 3rd ed. p. 398.
- [19] H.K., Versteeg and W. Malalasekera: “An introduction to Computational Fluid Dynamics, The Finite Volume Method”. Longman Scientific & Technical, United States of America, 1995, 1st ed.
- [20] Boiko A.V., Dovgal A.V., Grek G.R., Kozlov V.V., “The Origin of Turbulence in Near-wall Flows”, Springer-Verlag, 2002.
- [21] Finn E. Jørgensen: “How to measure turbulence with hot-wire anemometers-a practical guide” Dantec Dynamics, Denmark, 2002.
- [22] Web site: <http://www.dept.aoe.vt.edu/~simpson/aoe4154/hotwirelab.pdf>
- [23] Web site: http://en.wikipedia.org/wiki/Pressure_coefficient
- [24] Schlichting H., Boundary Layer Theory, McGraw-Hill, 1979.
- [25] R.B. Langtry and F. R. Menter: “Transition Modeling for General CFD applications in Aeronautics”, AIAA 2005-522, 2005.

APPENDIX

A. The test facility



B. Placement of the grid with respect to the model



C. Spanwise location of the probe

